RAYLEIGH LIDAR STUDIES OF THE ARCTIC MIDDLE ATMOSPHERE

By

Laura Jeanette Cutler

RECOMMENDED:

C. Sonnenwalker

Joseph S. Hawkins

Advisory Committee Chair

John Aspnes

Department Head

APPROVED:

D. Woodall

Dean, College of Science, Engineering and Mathematics

Dean of the Graduate School

8-28-00

Date

RAYLEIGH LIDAR STUDIES OF THE ARCTIC MIDDLE ATMOSPHERE

A

THESIS

Presented to the Faculty

of the University of Alaska Fairbanks

in Partial Fulfillment of the Requirements

for the Degree of

MASTERS OF SCIENCE

By

Laura Jeanette Cutler, B.S.

Fairbanks, Alaska

December 2000

Abstract

Rayleigh lidar allows us to measure density and temperature structure of the atmosphere at heights from approximately 35 to 80 kilometers. A Rayleigh lidar was installed at Poker Flat Research Range in November of 1997 and has been operated routinely since. This thesis presents an engineering analysis of the lidar system performance and a scientific analysis of the data obtained. The engineering analysis considers the receiver and transmitter alignment of the lidar system and the signal quality of the lidar data. The scientific analysis considers the retrieval of density and temperature profiles under a range of geophysical conditions. This study uses a three-year data set that includes 38 nights of data.

Table of Contents

List of Figures

List of Tables

List of Appendices

Acknowledgments

I wish to thank Dr. Richard Collins for inviting me to attend University of Alaska Fairbanks graduate school, for suggesting this topic and for his guidance in his role as my advisor. I would also like to thank Drs. Hawkins and Sonwalkar for serving on my graduate committee. I am grateful to Dr. Mizutani and Dr. Itabe of the Communications Research Laboratory in Tokyo, Japan for their support of the Rayleigh lidar at Poker Flat Research Range that made my study possible. I want to thank Justin Breese and Keith Nowicki for the many hours spent obtaining lidar data. Lastly, I gratefully acknowledge the support and encouragement from all my friends and family.

Dedication

To my parents: Richard and Virginia Cutler, for their never-ending encouragement and support in all that I endeavor.

Chapter 1: Introduction

1.1 Rayleigh Lidar and the Middle Atmosphere

The middle atmosphere is the region from about 15 km to 110 km as shown in Figure 1.1. The temperature profile is plotted on the left while the altitude distribution of several phenomena is shown on the right. The middle atmospheric region includes the stratosphere, mesosphere and lower thermosphere. One of the most important constituents in the middle atmosphere is ozone, which is the only atmospheric species to shield the biosphere from exposure to harmful radiation. While there is much interest in ozone, there is also much renewed interest in the middle atmosphere based on long-term climate change and short-term changes due to volcanic eruptions [Solomon, 1999]. Studies of this region have often been difficult due to limitations in instrumentation. Meteorological balloons can reach altitudes of up to 30 km before they pop, preventing measurements above this altitude. Radar can only make measurements up to about 30 km or above 70 km, due to the lack of scattering media (i.e., water molecules and electrons) in the middle atmosphere. Airglow measurements are confined to the naturally luminous layers above 80 km. Satellites can only make measurements of regions far above the mesosphere. So, there is a region from about 35 km to 80 km where there are relatively few routine measurements being made.

Rayleigh lidar systems are so named as they use the Rayleigh scatter from air molecules. Thus, in an atmosphere free of clouds and aerosols, the lidar signal is proportional to the density of the atmosphere. A lidar type approach involving a searchlight was first proposed in 1930 by Synge [Synge, 1930]. In 1951, Elterman implemented one of the first Rayleigh lidar-type approaches that

could reach the stratosphere by using a searchlight to measure the stratospheric density distribution (10-70 km) [Elterman, 1951]. The first experimental Rayleigh lidar using a laser was demonstrated in 1970 [Kent and Wright, 1970]. Soon after, a systematic approach was developed by Hauchecorne and coworkers, which showed improved accuracy over the previous approach [Hauchecorne and Chanin, 1980]. Currently, Rayleigh lidars are widely used in studies of the middle atmosphere, particularly in the height range 30 km to 80 km, which is aerosol free. Long-term observations have been ongoing at the Observatoire de Haute Provence (OHP) in France (44°N, 6°E) and at the Jet Propulsion Laboratory (JPL) Table Mountain Facility (TMF) in the United States (34.4°N, 117.7°W) [LeBlanc, 1998]. These observations have yielded studies of both long-term trends as well as short-term waves and tides [LeBlanc et al., 1997]. A highlight of the OHP observations is the detection of a statistically significant long-term temperature trend in the stratosphere and mesosphere. Analysis of the data set has yielded a cooling of 0.4 K/year in the mesosphere and 0.1 K/year in the stratosphere over a 20-year period [Keckhut et al., 1995]. Short-term observations at Eureka, Canada (80°N, 86°W) have been made during winter and spring to study the thermal structure of the polar stratospheric vortex [Duck et al., 2000]. This study has yielded insights into the coupling between radiative and dynamic processes in the circulation of the middle atmosphere.

A significant advantage of Rayleigh lidar systems is the fact that the systems are relatively turn-key. These lidar systems typically employ powerful Nd:YAG lasers that are technologically mature and can be maintained and operated in a routine fashion [Hecht, 1992]. The receiver does not require wavelength tuning and so while daytime measurements require precise design (very narrow bandpass filtering around 532 nm to avoid counting sunlight), nighttime measurements are straightforward. The only physical assumption

concerning the method is that the atmosphere is in hydrostatic equilibrium, which is valid over the temporal (several hours) and spatial (several km) scales of the measurement [Chanin, 1984]. The other successful lidar technique for measuring middle atmosphere temperature is the Na-resonance Doppler temperature lidar that uses the hyperfine structure of Na atoms in the mesopause region (80-100 km) to determine the wind and temperature [Bills et al., 1991]. Currently, Rayleigh lidar measurements remain the only viable ground-based technique for routinely measuring stratospheric and mesospheric temperature profiles.

The Communications Research Laboratory (CRL) of Tokyo, Japan installed a Rayleigh lidar (light detecting and ranging) system at Poker Flat Research Range (PFRR) (65° N, 147° W) in November 1997. The Rayleigh lidar was installed by staff from the CRL as part of a collaborative effort between the Geophysical Institute (GI) and the CRL [Collins et al., 1998a;b]. It has been operated during the autumn, winter and spring of 1998, 1999 and 2000. Measurements are taken frequently during the fall, winter and spring months, but not during the summer months due to the fact that PFRR is located near the Arctic Circle and does not experience astronomical darkness (sun is 18° below horizon) in summer. From November 1997 to May 1999, the CRL lidar operated in the Optics Facility. From May 1999 to April 2000, it was operated in the Davis Science Center.

1.2 Scope of this Study

The goal of this study is to carry out an engineering analysis of the system performance and a scientific analysis of the initial observations. Standard engineering signal processing techniques are employed to assess the quality of the data. Biases in the data due to errors in the transmitter and receiver alignment will be considered and methods of screening the data will be

discussed. The retrieved temperature measurements will be presented in terms of the general structure of the stratosphere and mesosphere and in particular in terms of mesospheric inversion layers.

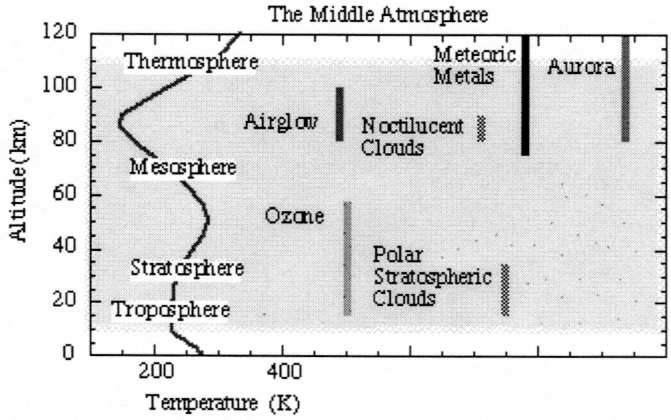

Figure 1.1: The atmospheric temperature profile and the altitude distribution of several atmospheric phenomena.

Chapter 2: Rayleigh Lidar Principles

2.1 Rayleigh Scattering

Lord Rayleigh discovered this phenomenon in 1871 and called it selective scattering [Rayleigh, 1871]. In general, scattering is a process where light is absorbed by a particle and then emitted in another direction. Rayleigh scatter occurs when radiation hits a spherical particle or molecule whose diameter is smaller than the wavelength of the radiation. Air molecules are small in size (~0.5 nm) and are therefore more effective at scattering light of shorter wavelengths such as blue and violet (~400 nm) than red (~700 nm), which is why the sky appears blue.

Rayleigh scattering is found to be inversely proportional to the wavelength to the fourth power. The intensity of the light is proportional to the molecule's vibration squared, which is in turn proportional to the acceleration squared. Rayleigh has shown this acceleration to be:

$$-A\left(\frac{2\pi c}{\lambda}\right)^2 \cos\left(\frac{2\pi ct}{\lambda}\right), \tag{2.1}$$

based in part on Stokes' Theory of Diffraction [Stokes, 1849]. By squaring the above acceleration term to come up with the intensity, the $1/\lambda^4$ dependency is apparent. By using more modern concepts such as a simple radiating dipole, similar results are found [e.g., Kong, 1986].

2.2 The CRL Rayleigh Lidar System at PFRR

As mentioned in the introduction, the CRL installed a lidar system at Poker Flat Research Range (PFRR) in November 1997. A diagram of the lidar system is provided in Figure 2.1. At midnight during the summer solstice, the sun is less

than 2° below the horizon. There is no astronomical darkness (sun is 18° below horizon) between April 7 and September 4 and no civil twilight (sun is 6° below horizon) between May 15 and July 27. The CRL Rayleigh lidar is unable to take data during the summer months; however, lengthy data sets can be taken during the long winter nights.

The lidar may be divided into several main components for both the receiver and transmitter. The transmitter consists of a laser, a beam expander, a beam steering mirror and a laser pulse detector (LPD). The receiver consists of a telescope, a photo multiplier tube (PMT), a high-speed counter and a computer. A detailed block diagram of the receiver system is shown in Figure 2.2. The CRL system laser is a Nd:YAG Continuum® Powerlite 8000 laser which emits at a wavelength of 532 nm. More details are provided in Table 2.1.

Table 2.1: Specifications of Nd:YAG laser at PFRR.

Repetition Rate	20 Hz
Energy (at 532nm)	550 mJ
Pulsewidth	5-7 ns
Linewidth	1.0 cm^{-1}
Divergence	0.45 mrads
Beam pointing stability	+/- 30 µrads
Jitter	+/- 0.5 ns
Energy stability	3.5
Power drift	+/- 5.0%
Beam spatial profile	0.7
Max deviation from fitted Gaussian	+/- 40%

The laser is a Q-switched laser to allow a large pulse to be generated. Once that pulse is transmitted, a pulse detector senses it and sends a signal to

the high speed counter. The high speed counter, called a multichannel scalar (MCS), counts the incoming PMT pulses in a given time window at rates up to 150 MHz. By successively counting the pulses in a sequence of time windows the MCS forms a profile in time, which is converted to altitude knowing the speed of light. For a 75 m resolution profile the time bins are 0.5 μs. The next laser pulse triggers the MCS and the new profile is added coherently to the previous one. The process continues for a predetermined number of laser shots, typically 2000, and the final integrated profile is transferred to the PC. A set of these profiles, typically 16, is then stored in a data file. The observation for each night is a sequence of these sets. Because there is so much scattering in the atmosphere below 30 km, the receiver is electronically gain switched so that photons returned before 150 μs (corresponding to 22.5 km) are not counted. On January 24, 2000, tests were performed to record the timing between the various components. When the Q-switch triggers there is a 40 ns delay after the pulse detector senses the pulse and accordingly sends its signal out. There is a 65 ns delay between the laser pulse detector and the MCS unit turning on. These findings are summarized in Figure 2.3.

2.3 The Lidar Equation

Rayleigh lidar uses the light Rayleigh scattered from molecules in the atmosphere to produce a profile of relative density. The returned photon count signal is proportional to the density of the atmosphere. The expected photon count from an altitude range ($z-\Delta z/2$, $z+\Delta z/2$) in a time interval Δt is given by the lidar equation:

$$N(z) = N_S(z) + N_B + N_D, \tag{2.2}$$

where $N_s(z)$ is the signal count proportional to the atmospheric density:

$$N_S(z) = \eta T^2 \frac{E_L R_L \Delta t}{hc/\lambda_L} \rho(z) \Delta z \sigma_\pi^R \frac{A_T}{z^2}, \tag{2.3}$$

N_B is the background skylight count:

$$N_B = \eta [H_N R_L \Delta t \pi (\Delta\Theta_R / 2)^2 A_T \Delta\lambda] (\frac{2\Delta z}{c}) / (\frac{hc}{\lambda}) \tag{2.4}$$

and N_D is the detector dark count:

$$N_D = (C_N R_L \Delta t)(\frac{2\Delta z}{c}). \tag{2.5}$$

In the lidar equations above, η is the receiver efficiency, T is the atmospheric transmission at the transmission wavelength λ_L (m), E_L is the laser energy per pulse (J), R_L is the repetition rate of the laser (s^{-1}), $\rho(z)$ is the concentration of scatterers at altitude z (m^{-3}), σ_π^R (m^2) is the effective backscatter cross section at λ_L, h is Planck's constant (~6.63×10^{-34} J s), c is the speed of light (~3×10^8 m/s), A_T is the area of the telescope (m^2), H_N is the background sky radiance ($W/(m^2\ \mu m\ sr)$), $\Delta\Theta_R$ is the field of view (FOV) of the receiver (rad), $\Delta\lambda$ is the bandwidth of the detector (μm) and C_N is the dark count rate for the detector (s^{-1}). N_D and N_B are expected constant with height and their sum can be determined from the signal at the highest altitudes (>100 km) where $N_S(z)$ is negligible. The fundamental source of error is the Poisson distribution associated with the expected value [Papoulis, 1984]. The uncertainty in a given measurement is given as

$$\Delta N_S(z) = (N_S(z) + N_D + N_B)^{1/2}. \tag{2.6}$$

Once the signal photon count has been determined, the ratio of the signal photon count from two altitudes is used to yield the range scaled relative density profile:

$$\frac{N_S(z_1)}{N_S(z_2)} = \frac{\rho(z_1)}{\rho(z_2)} \left(\frac{z_2}{z_1} \right)^2, \tag{2.7}$$

where $\rho(z)$ is the molecular density at altitude z and $N(z)$ is the photon count from altitude z. This relationship is accurate for altitude ranges above the troposphere where the atmospheric transmission is constant with increasing altitude. The relationship also normalizes out all the system specific parameters such as receiver efficiency laser energy and telescope area. This is the basic principle of the Rayleigh lidar technique in that it yields an accurate measure of the relative density profile.

The hydrostatic approximation

$$\frac{dp}{dz} = -\rho(z)g(z) \tag{2.8}$$

and ideal gas law

$$P = \frac{\rho RT}{M} \tag{2.9}$$

(where P is the atmospheric pressure, ρ is the atmospheric density, R is the ideal gas constant and M is the molecular weight of the gas) can be combined as

$$P(z) = -\int_{z_0}^{z} \rho(r)g(r)dr + \frac{R}{M}\rho(z_0)T(z_0) \tag{2.10}$$

$$= \frac{R}{M}\rho(z)T(z)\,. \tag{2.11}$$

Hence,

$$T(z) = \frac{\rho(z_0)}{\rho(z)}T(z_0) - \frac{M}{R}\int_{z_0}^{z}\frac{\rho(r)}{\rho(z)}g(r)dr\,. \tag{2.12}$$

The temperature profile is actually calculated by integration downward from an initial estimated temperature using:

$$T(z) = T(z_0)\frac{N(z_0)}{N(z)}\left(\frac{z_0}{z}\right)^2 + \frac{M}{R}\int_{z}^{z_0}\frac{N(r)}{N(z)}\left(\frac{r}{z}\right)^2 g(r)dr \tag{2.13}$$

where g is the gravitational constant, M is the mean molecular mass of dry air, R is the universal gas constant and $N(z)$ is synonymous with $N_S(z)$. For a series of range bins, the integration becomes a summation from the top (bin 1) downward:

$$T_i = \frac{T_1 N_1 z_1^{\,2}}{z_i^{\,2} N_i} + \frac{M}{R} \Delta z \sum_{j=2}^{i} \frac{N_j g_j z_j^{\,2}}{z_i^{\,2} N_i}. \qquad (2.14)$$

As $N(z)$ decreases with height the first term increases and the sensitivity to the initial temperature estimate reduces as we integrate downward. The integration starts at a top seed altitude and the profile progressively converges to the true temperature. Various comparisons have been published showing both the convergence of the Rayleigh lidar temperature profile from above to a radiosonde temperature profile from below [e.g., Collins et al., 1992] and the comparison between two closely located lidars [Hauchecorne et al., 1991]. Since atmospheric models are used in comparison with the PFRR data, some assumptions were tested. The validity of the hydrostatic equilibrium assumption in various atmospheric models is discussed in Appendix A. A more general testing of the model atmospheres using the Rayleigh lidar technique is discussed in Appendix B.

A basic Rayleigh lidar measurement is shown in Figure 2.4. Figure 2.4a shows a photon count profile that decays with altitude up to 90km as the density of the atmosphere decreases. Above 90 km, the lidar signal is dominated by background light. Below approximately 25 km, the lidar receiver is electronically gain switched to avoid overloading the detector. Large signals from these low altitudes yield photon count rates that are too fast for the detector's pulse counter. These large signals also demand large currents from the high voltage power supply and yield a varying detector gain with altitude that distorts the lidar return. Finally, overloading of the detector can also cause signal-induced noise in the detector that varies with altitude and corrupts the estimate of the signal

photon counts (i.e. N_D varies with altitude). Figure 2.4b shows a retrieved temperature profile with a stratopause maximum near 50 km with secondary maximum in the mesosphere. The profile has been integrated downward from an initial temperature at 80 km. The quality of the data clearly decreases with altitude. An error of 25 K is assumed in the initial seed temperature at 80 km. The error is calculated for each 75 m-range bin (the fundamental data bin). Reducing the resolution of the measurements would reduce the error accordingly (see Appendix C).

While the technique is straightforward, there are a variety of ways in which the relationship is invalid. The telescope FOV must cover the laser beam at all altitudes. If this is not the case, then an overlap function that is the fraction of the laser beam in the telescope FOV must be included. This is discussed in the Chapter 3. Large returned lidar signals, typically from lower altitudes, will yield overloading of the detectors and artificially low photon counts.

2.4 Spectral Analysis of the Data

The model for the lidar photon count data is a deterministic signal (i.e., the expected photon count is proportional to the atmospheric density profile) plus an additive white noise due to the statistical nature of the photon counting process. From the lidar equation, the relative statistical uncertainty in the data is given by:

$$\frac{\Delta N_S}{N_S} = \frac{\sqrt{N_S + N_D + N_B}}{N_S}, \tag{2.15}$$

which decreases with increasing N_S. Thus, the uncertainty can be modeled as an additive noise that is uncorrelated between range bins. Small-scale features in the data profiles (e.g., a small maximum or minimum that extends over 1km in altitude) need to be identified as either geophysical features or artifacts of the

noise. To study which components of the measured signal (geophysics or noise) dominate at given scale spectral analysis is used.

The FFT is an algorithm designed to compute efficiently an N-point discrete Fourier transform (DFT). This type of spectral analysis tool provides information how the power or energy in the signal varies as the function of frequency. Normally a time series is used and the FFT converts it to a series in the frequency domain. In this case, the time series is replaced by photon count data at corresponding altitudes. In essence, it is an altitude series. When the FFT is taken of this altitude series, the resulting spectrum is a function of inverse wavelength or wavenumber. The wavelength is expressed in km^{-1} or inverse kilometers. The absolute value of the FFT was then squared to create a periodogram. The periodogram method is used to determine the spectrum of the lidar photon count signal [Blackman and Tukey, 1958]. This periodogram is then normalized to 0 dB at DC.

The total noise power is proportional to the total photon count as the amplitude of the noise fluctuation at each height range is proportional to the square root of the expected photon count. For good quality data, the spectrum is expected to be signal dominated at low wavenumbers and noise dominated at the high wavenumbers. If the spectrum is normalized by the signal spectrum value at DC normalized signal spectrum and a normalized noise floor are found. Thus it is expected that the normalized noise floor is proportional to the total relative error in the photon counts profile. To quantify the behavior, the expected relative noise power was calculated from the square of equation 2.14.

To illustrate these ideas, the data from November 8, 1998 was considered. An integrated photon count profile over different time ranges was taken with different altitude ranges to look at varying signal to noise ratios. Then the periodogram was found for these different cases. The results are shown in Figure 2.5. The photon count spectrum is denoted by the thin curve, the

smoothed spectrum is denoted by the thick curve, the estimated noise floor is the thin flat line and the thin dashed line denotes 3dB above the noise floor. The periodogram noise floor was calculated by the assumption that the noise will dominate at scales less than 200 m (or greater than 5.0 km^{-1} on the periodogram). Note that the periodograms end at 6.66 km^{-1}; this corresponds to the Nyquist wavenumber of the data (corresponding to the altitude range bin resolution of 75 m). In Figure 2.5a the profile is integrated over 5 minutes of data in the 65-80 km altitude range. The noise floor is clearly visible at wavenumbers greater than 2 km^{-1}. This indicates for measurements at 5 minute resolution on November 8, 1998 features at scales less than 500 m are not geophysically significant. Note for this case where there is a small number of photon counts, the noise floor and the expected noise power are in good agreement, the calculated noise floor is –36 dB while the measured spectral noise floor is –38 dB. In Figure 2.5b the effective number of photon counts is increased by considering the same altitude range (65-80 km), but increasing the time to a 2 hour period (i.e. larger Δt in the lidar equation). In this figure, the noise floor at the higher wavenumbers is starting to include signal. This is reflected in the fact that the expected photon count noise power (-50 dB) is 7 dB lower than the spectral assumed noise floor (-43 dB). In Figure 2.5c the effective number of photon counts is increased again by including data from the entire night (about 10 hours) over the altitude range 65-80 km (i.e. larger Δt in the lidar equation). The signal component is now obviously dominating the spectrum at all wavenumbers; accordingly, the expected noise power (-57 dB) decreases further below the assumed noise floor (-43 dB). In Figure 2.5d the photon count profile extends in altitude from 35-80 km and over the entire 10 hour observation period (i.e. larger Δt, $\rho(z)$ in the lidar equation), making this the largest number of photon counts. For this spectrum, no white noise floor is seen as the spectrum decays from the maximum at DC to the highest wavenumbers. The expected

noise power (-80 dB) is significantly lower than the assumed noise floor (-42 dB). Clearly, the signal is dominating the spectrum at even the highest wave numbers, and the photon count noise floor and the spectral noise floor do not agree and differ by 38 dB. For the final three cases the spectrum is increasingly signal dominated at the high wavenumbers. This is demonstrated by the fact that the spectral noise floor estimate stays constant at about –42 dB, indicating a constant power at these higher wavenumbers. A summary of the results discussed regarding Figure 2.5 is provided in Table 2.2.

Table 2.2: Summary of FFT data for the night of November 8, 1998.

altitude (km)	Figure	total number of laser shots	total number of photon counts	periodogram noise floor (dB)	photon relative noise level (dB)
65-80, 5 min. bins	2.5a	6.0e3	4.6e3	-38	-36
65-80, 2 hr bins	2.5b	1.4e5	1.1e5	-43	-50
65-80, entire night	2.5c	6.3e5	5.0e5	-43	-57
35-80, entire night	2.5d	6.3e5	1.1e8	-42	-80

2.5 Conclusions

The periodogram proved to be an important tool, providing information on the optimal smoothing length to use for analyzing the lidar data. The analysis shows that the data follows a Poisson photon count model. The method allows the smallest scales that are geophysically significant to be determined for a given resolution measurement. This is important in ensuring consistency in the features reported from different nights when the signal quality may vary significantly with sky clarity and atmospheric transmission. For the work in this thesis, the data is conservatively low pass filtered at a wavenumber of 0.5 km^{-1} (2 km). This is to ensure consistency across all data sets where there may be varying noise and signal power levels. The error in the temperature due to this photon count noise is calculated in Appendix C.

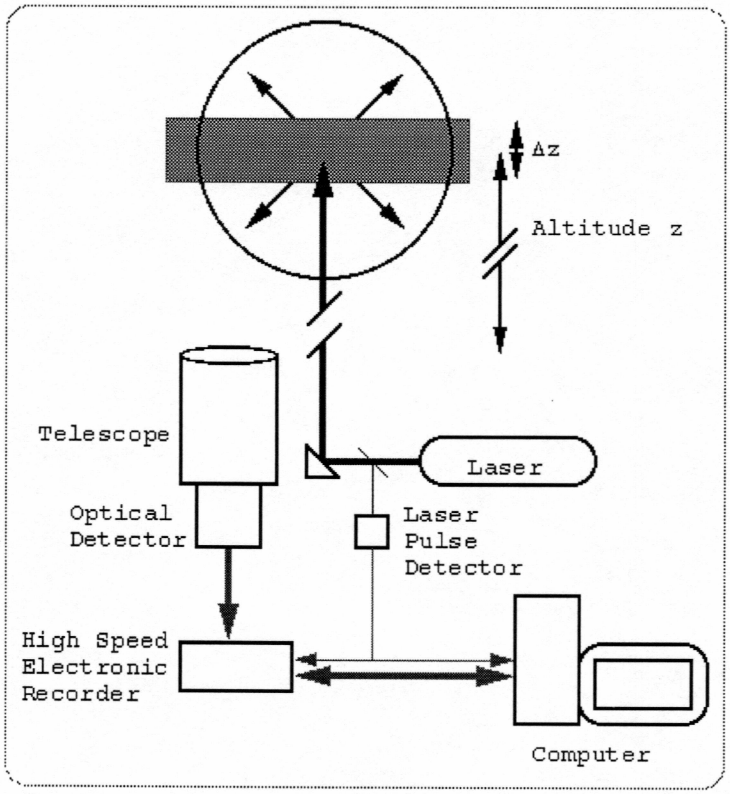

Figure 2.1: CRL Rayleigh lidar system at PFRR.

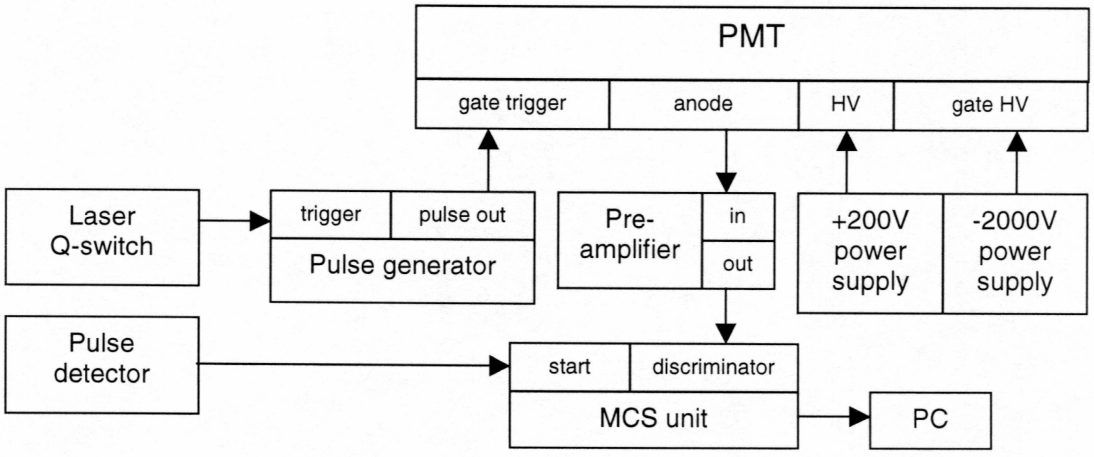

Figure 2.2: Block diagram of CRL Rayleigh lidar receiver at PFRR.

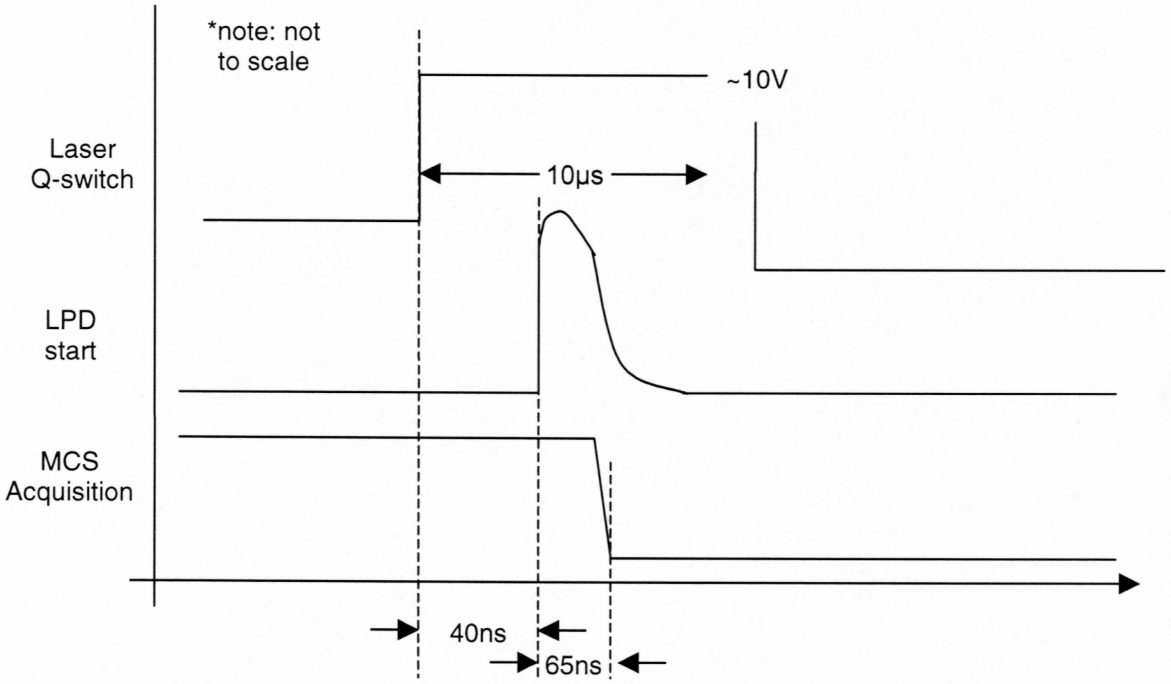

Figure 2.3: Timing diagram of CRL Rayleigh lidar at PFRR.

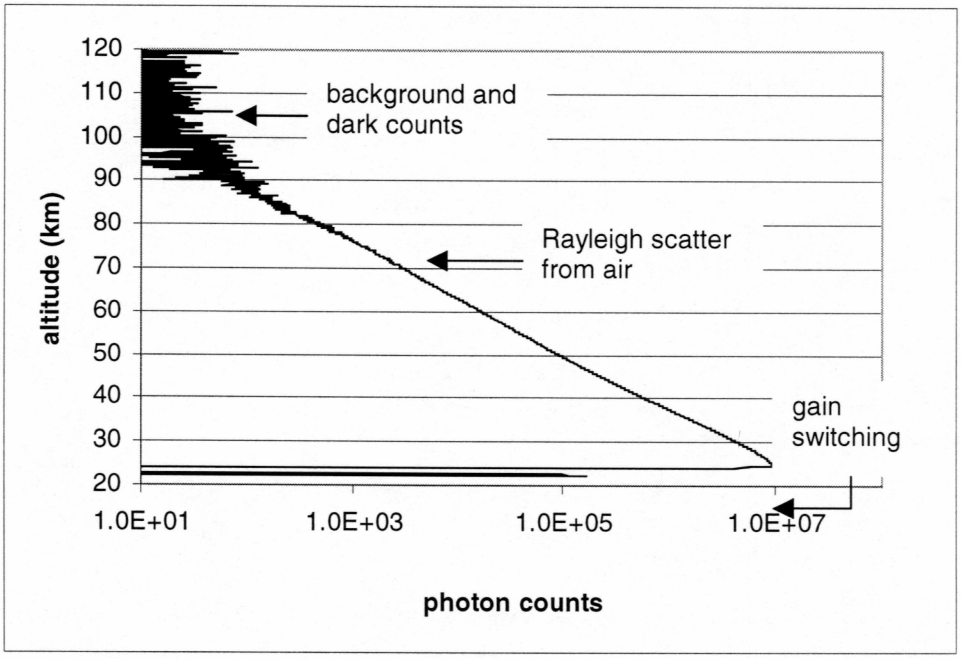

Figure 2.4a: Typical photon counts received by Rayleigh lidar.

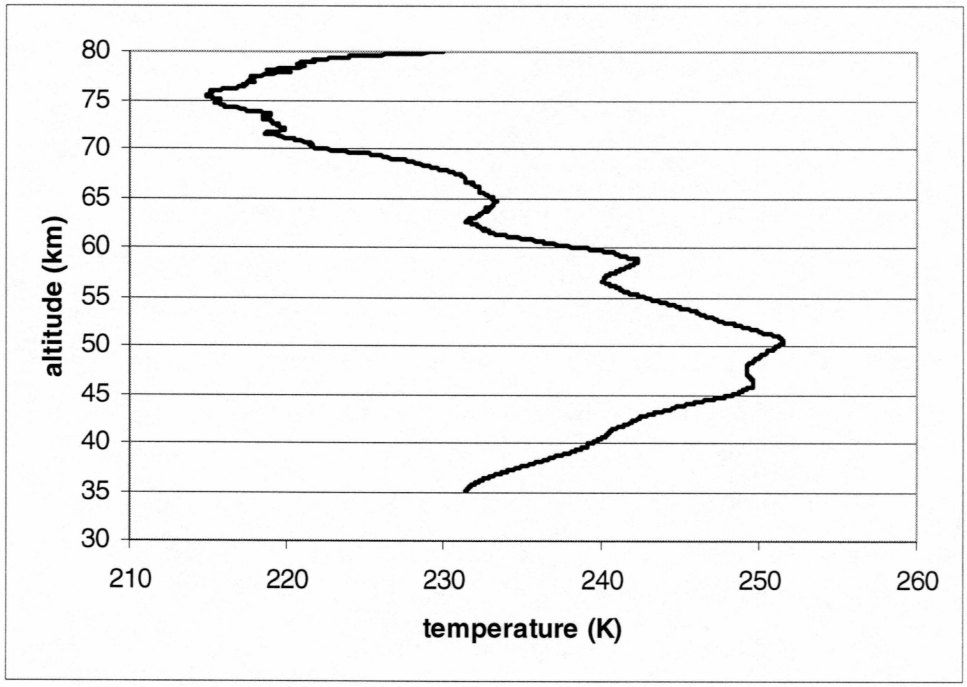

Figure 2.4b: Typical temperature measurement retrieved from photon counts.

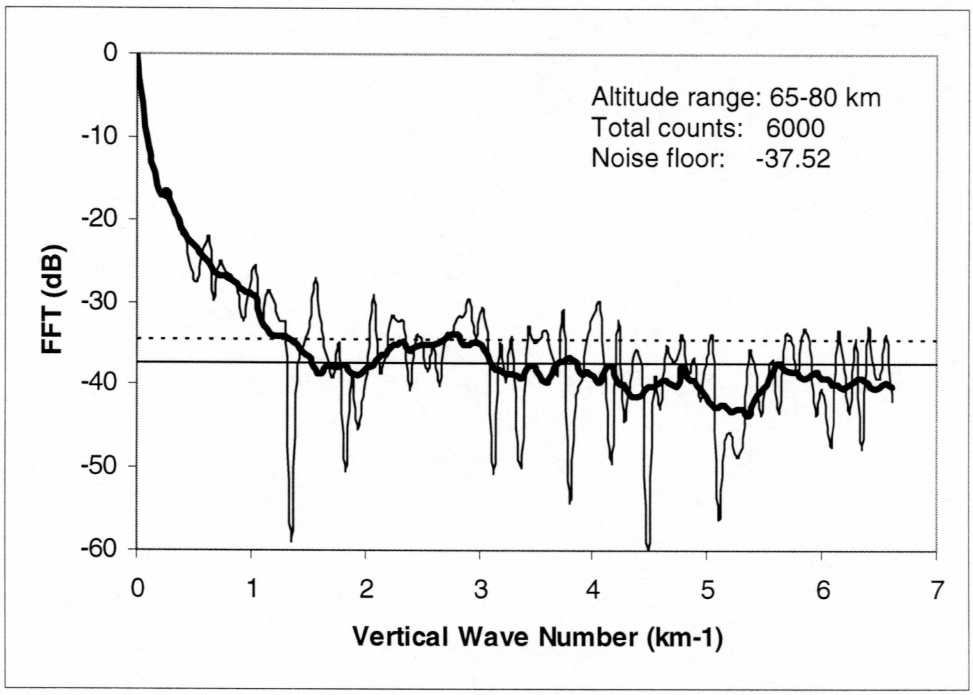

Figure 2.5a: FFT of 5-minute bins of data for November 8, 1998 from 65-80 km.

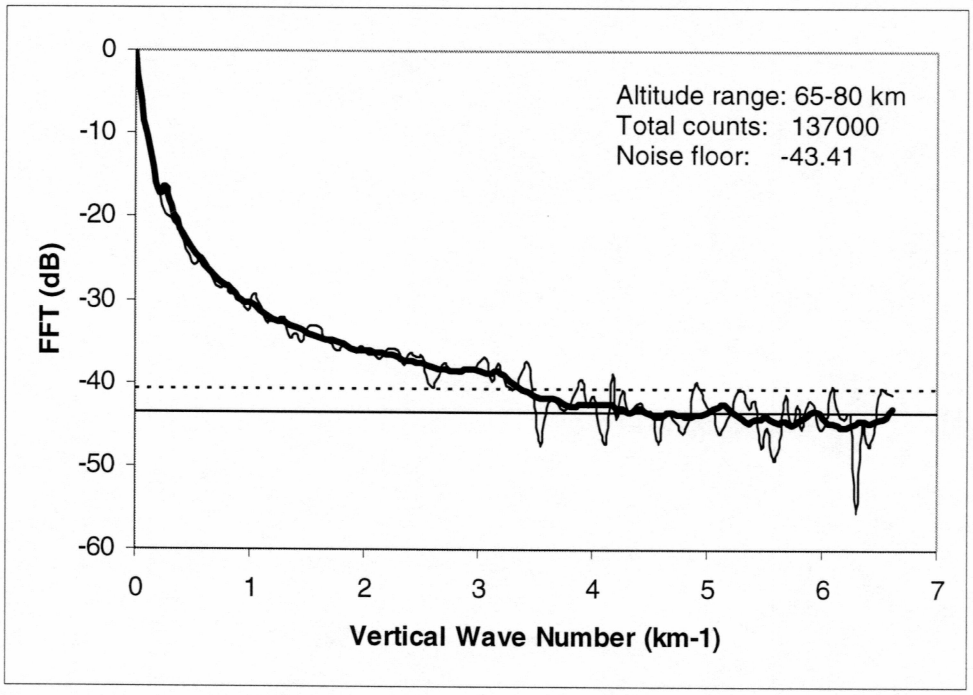

Figure 2.5b: FFT of 2-hour bins of data for November 8, 1998 from 65-80 km.

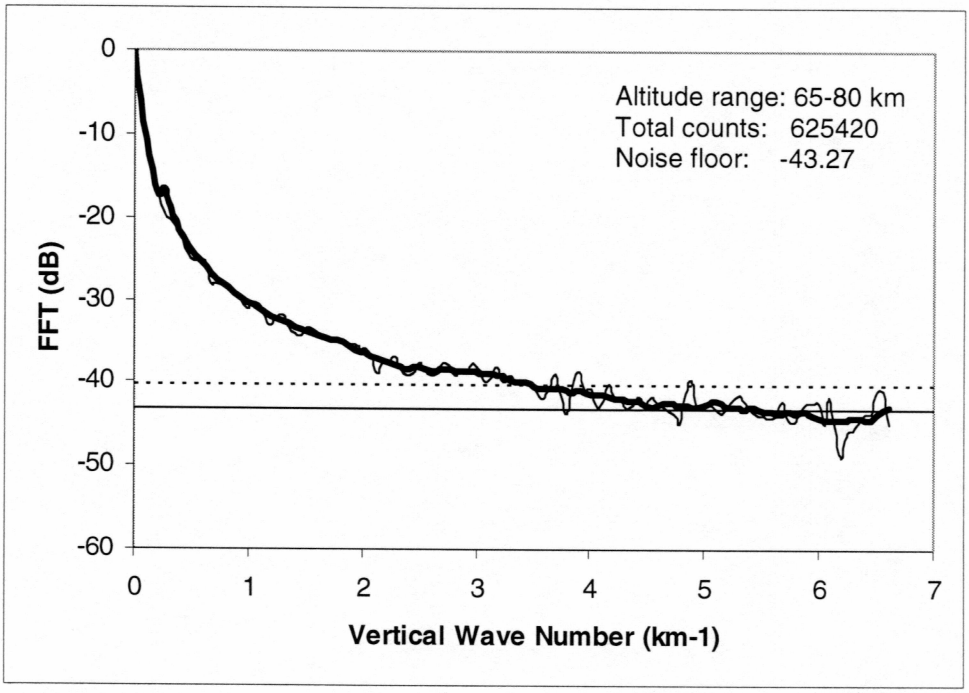

Figure 2.5c: FFT of entire night of data for November 8, 1998 from 65-80 km.

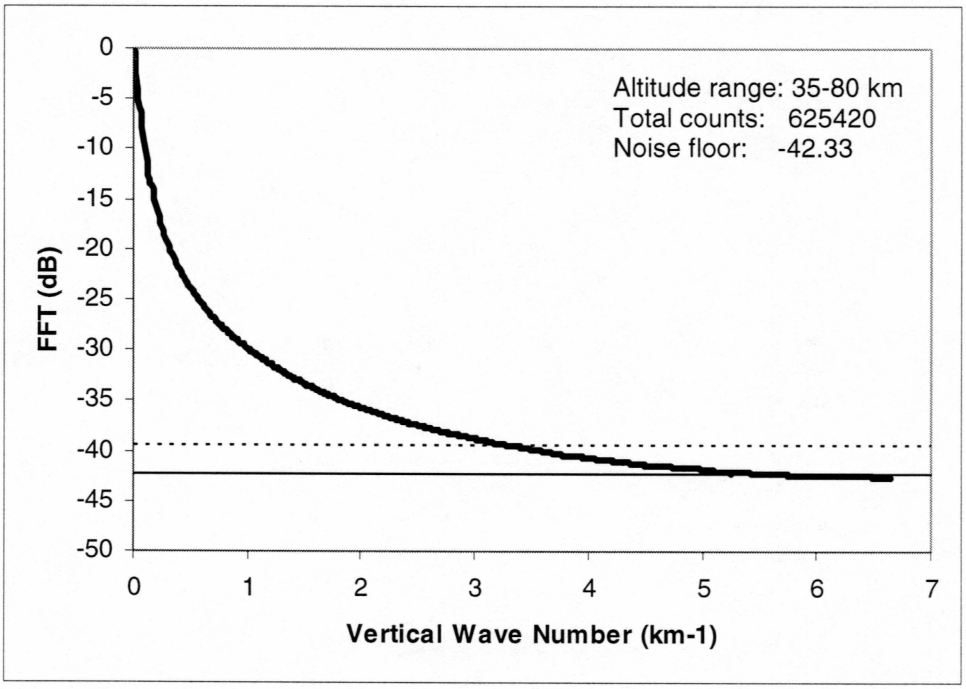

Figure 2.5d: FFT of entire night of data for November 8, 1998 from 35-80 km.

Chapter 3: Beam Steering

3.1 Introduction

Alignment of the telescope and laser is critical in making accurate measurements. The transmitter of the lidar, the laser, illuminates a spot in the sky. For a bistatic system, the telescope sees the laser if the spot falls within the telescope field-of-view (FOV) as seen in Figure 3.1. The alignment of the laser and telescope is described by an overlap model, $\xi(z)$, which modifies the signal term in the lidar equation (Equation 2.3) as follows:

$$N(z) = \xi(z)\eta T^2 \frac{E_L R_L \Delta t}{hc/\lambda_L} \rho(z) \Delta z \sigma_\pi^R \frac{A_T}{z^2}. \tag{3.1}$$

$\xi(z)$ can be defined as:

$$\xi(z) = \frac{N(z)}{M(z)}, \tag{3.2}$$

where $N(z)$ is the actual lidar signal and $M(z)$ is the expected lidar signal when the laser and telescope are perfectly aligned. Clearly, the overlap model will affect the retrieval of temperatures as:

$$\frac{N(z_1)}{N(z_2)} \frac{{z_1}^2}{{z_2}^2} = \frac{\rho(z_1)\xi(z_1)}{\rho(z_2)\xi(z_2)}. \tag{3.3}$$

If the fraction of the overlap model is determined, then the data may be compensated and provide an accurate temperature profile. When mentioned in the literature, the authors usually state that it is negligible and do not address it directly [e.g., LeBlanc, et al., 1998].

Considered in this chapter are the geometry for zenith pointing lidar systems and the geometry for systems where the laser is tilted relative to the telescope. Operational methods for aligning the laser and telescope are also

discussed. The expected effect on temperature retrievals of typical misalignments is calculated. Finally, typical data from PFRR is presented.

3.2 Geometry of the Problem

First, a basic set of formulas is determined for how much the laser beam overlaps with the telescope FOV at any height. The assumptions are that the laser beam and telescope FOV are circular spots (i.e., there is no tilt to the telescope or laser) and that the laser beam is uniform. The area where they overlap is called the spot size. In order to determine the spot size, the geometry of a pair of circles with portions that overlap is considered. Figure 3.2 gives the area of the portion of the circle cut off by the chord. Figure 3.3 shows how the laser beam and telescope FOV might overlap at any given height below z_2 (as shown in Figure 3.1).

In order to solve for the overlapping areas of the laser and telescope, the most important pieces of information needed are the angles, α_L and α_T. The only variables known are the separation distance, d, the telescope FOV, θ_T, and the laser beam divergence, θ_L. The variable, *dxtc*, is defined as the distance between the chord common to both the laser and telescope circular areas and the center of the telescope FOV. The variable, *dxlc*, is defined as the distance

$$
\begin{aligned}
r_T &= z\tan(\Theta_T/2) \\
r_L &= z\tan(\Theta_L/2) \\
dxtc &= x_R - x \\
dxlc &= x \\
\alpha_L &= 2\cos^{-1}(dxlc/r_L) \\
\alpha_T &= 2\cos^{-1}((dxtc/r_T) \\
A_T &= \tfrac{1}{2}\, r_T^2(\alpha_T - \sin\alpha_T) \\
A_L &= \tfrac{1}{2}\, r_L^2(\alpha_L - \sin\alpha_L) \\
A_{spot} &= A_T + A_L.
\end{aligned}
\qquad (3.4 - 3.12)
$$

between the chord common to both the laser and telescope circular areas and the center of the laser beam divergence. The radii of the spot sizes of the laser and telescope at any altitude, z, are denoted as r_L and r_T, respectively. With

these definitions, the result is the set of formulas 3.4 – 3.12. As shown, the area of the spot is given as the sum of the two portions $A_L + A_T$. After the area of the spot size is determined, a short program takes in the following information: the distance between the laser and the telescope, the telescope FOV and the laser beam divergence. From this information the spot size is calculated as a function of height. The program also calculates what the spot size of the laser beam is as a function of height. Knowing these two quantities, the ratio of spot size to laser beam spot size as a function of height to be calculated. This ratio is the overlap model:

$$\xi(z) = \frac{A_T + A_L}{\pi r_L^{\,2}} \tag{3.13}$$

which varies between one and zero. This overlap model shows how much the laser beam overlaps with the telescope FOV as a function of height. If the ratio is one, then there is full overlap and the telescope can see the entire return signal. If the ratio is zero, then the laser beam is not inside the telescope FOV at all and no signal can be received.

3.3 Operational Geometry

So far, the overlap function, $\xi(z)$, has been determined for the special case where the laser and the telescope were both pointed vertical. In this section, various cases where the laser and the telescope are tilted relative to one another are considered. The case of the zenith pointing (fixed) telescope and tilted laser (both away and toward the telescope) is considered. Then, the case of a tilted laser and a tilted telescope is considered. Finally, the effects of the FOV of the telescope and the laser beam divergence will be considered. For all these cases the physical parameters are based on the Optics Facility, specifically d = 6 m, Θ_T = 1.0 mrad and Θ_L = 560 μrad.

3.3a Laser Tilted in the Zenith Plane of the Laser and Telescope

When the laser is tuned and the optics are aligned, it is not guaranteed that the laser is perfectly vertical. The zenith plane is defined as the vertical plane through the base of the telescope and laser beam. An angle at the base of the laser is introduced and overlap model is recalculated. This angle is known as the laser's "tilt" and is labeled as φ_x in Figure 3.1. Table 3.1 shows the worst case φ_x based on a known z_3 (Figure 3.1). This φ_x is quite small,

Table 3.1: The small variances of φ_x.

	d(m)	$\Delta\Theta_T$(mrad)	$\Delta\Theta_L$(μrad)	Z_3 (km)	φ_x (μrad)
Optics Facility	6	1	560	40	370
	6	1	560	60	320
	6	1.5	560	40	620
	6	1.5	560	60	570
Davis Science Center	15	1.5	560	40	510
	15	1.5	560	60	500

but has a large impact due to the large altitude ranges; the equations that were determined in the original problem must be reconsidered. Taking into account the tilt of the laser beam, it now must be considered what happens when the laser beam starts to move out of the telescope FOV on the far side of the telescope FOV. Figure 3.4 shows how the laser beam might move across the telescope FOV as the altitude increases. The result is an equation set (3.14 – 3.24) similar to the previous case but more complicated due to different

$$
\begin{aligned}
r_T &= (z\Theta_T)/2 \\
r_L &= (z\Theta_L)/2 \\
\Phi_x &= \tan^{-1}((d + z_s(\tan(\Theta_T/2)-\tan(\Theta_L/2)))/z_s) \\
x_R &= d - x\Phi_x \\
dxtc &= x_R - x \\
dxlc &= x \\
\alpha_L &= 2\cos^{-1}(dxlc/r_L) \\
\alpha_T &= 2\cos^{-1}(dxtc/r_T) \\
A_T &= \tfrac{1}{2}\, r_T^2(\alpha_T - \sin\alpha_T) \\
A_L &= \tfrac{1}{2}\, r_L^2(\alpha_L - \sin\alpha_L) \\
A_{spot} &= A_T + A_L.
\end{aligned}
\qquad (3.14 - 3.24)
$$

geometry. Because the distance between the laser and the telescope changes with height due to the tilt of the laser beam, a new variable, x_R, is introduced. In the zenith pointing case, x_R equals d, but in general x_R is the separation of the laser beam and telescope FOV centers at any height as seen from the ground. These new equations reduce to the first set for zenith pointing case when $\varphi_x = 0$. The radius of the laser beam and the radius of the telescope should also change through the tilt, but the effect is negligible. Also, the tangents of many of the angles have been omitted because the angles are very small and the tangent of a small angle can be represented as just that angle. The program mentioned in the previous section was modified to incorporate the idea of tilt in the laser beam. Theoretical tilted overlap models are shown in Figure 3.5 for a variety of steering altitudes.

This case of overlap with tilt in one direction is also discussed in Measures [Measures, 1984]. His equations are:

$$\begin{aligned} \alpha_L &= \cos^{-1}[(d^2+r_L^2-r_T^2)/2r_L d] \\ \alpha_T &= \cos^{-1}[(d^2- r_L^2+r_T^2)/2r_T d] \\ A &= r_L^2\alpha_L + r_T^2\alpha_T - r_T d\sin\alpha_T \end{aligned} \qquad (3.25 - 3.27)$$

The equations in this thesis were derived independently of Measures, but can readily be shown to be equivalent.

3.3b Tilted Overlap Away from the Telescope

One last case of overlap needs to be considered. This is the case that the laser beam is tilted away from the telescope. Due to the nature of this problem, only the tilt in the x direction was considered. The tilt angle, φ_x, is used as it was in the one direction tilting problem. Note, however, that φ_x is now negative since $\varphi_x = 0$ is vertical. The overlap program created for tilt in one direction was used to demonstrate the effects of a negative φ_x. Various overlap models for this case are shown in Figure 3.6. As expected, the altitude where partial overlap begins increases with the tilting angle of the laser. Furthermore, the telescope FOV,

which is wider than the laser beam divergence, eventually covers the whole laser beam and the overlap model tends to 1 with altitude.

3.3c Laser Tilted out of the Zenith Plane

In the previous sections, tilted overlap in one direction (positive and negative) was presented. This case is limited to the laser beam being tilted across the exact center of the telescope FOV. As shown in Figure 3.7, the laser beam could be tilted in essentially two directions. Figure 3.8 demonstrates how the laser beam would move across the telescope FOV if it were tilted in two directions. To denote this tilt, a new variable, φ_y, is introduced. At the steering altitude, the laser beam is in a different x location in this case than it was in the case presented previously; and therefore, φ_x, has to be modified. However, it still denotes the tilt in the x direction. The equations for finding the area of the spot size in this case are:

$$
\begin{aligned}
r_T &= (z\Theta_T)/2 \\
r_L &= (z\Theta_L)/2 \\
\Phi_x &= d/z_s \\
\Phi_y &= \Theta_T/2 - \Theta_L/2 \\
x_R &= sqrt((d - z\Phi_x)^2 + (z\Phi_y)^2) \\
dxtc &= x_R - x \\
dxlc &= x \\
\alpha_L &= 2cos^{-1}(dxlc/r_L) \\
\alpha_T &= 2cos^{-1}(dxtc/r_T) \\
A_T &= \tfrac{1}{2}\, r_T^2(\alpha_T - sin\alpha_T) \\
A_L &= \tfrac{1}{2}\, r_L^2(\alpha_L - sin\alpha_L) \\
A_{spot} &= A_T + A_L
\end{aligned}
\qquad (3.28 - 3.39)
$$

Again, the overlap program was modified to account for tilt in two directions; the resulting overlap models are shown in Figure 3.9.

3.3d Varying the Telescope FOV and Laser Beam Divergence

Another analysis performed on the overlap model is to see how it varies as a function of the telescope FOV and the laser beam divergence. These overlap models were created using the case described in Section 3.3a. Figure 3.10 shows how the telescope FOV affects the overlap model. Θ_L was fixed at 560 μrad and Θ_T was varied from 1.0 to 1.5 mrad. Figure 3.11 shows how the laser beam divergence affects the overlap model. Θ_T was fixed at 1.5 mrad and Θ_L was varied from 520 to 560 μrad. In both cases, it is easy to see that the larger the telescope FOV and the larger laser beam divergence force the overlap model closer to one and therefore the data is less prone to error due to operational misalignment.

3.4 Effect on Temperature Retrieval

The next step is to see how these overlap models affect the temperature data. In this analysis, the MSISE temperature data for December 1990 was used. For the following set of overlap models, the numbers used are the ones consistent with usual data taking parameters in the Optics Facility. The telescope FOV is 1.0 mrad, the laser beam divergence is 470 μrad, the telescope to laser distance is 5.93 m and the steering altitude is varied. First, a simulated photon count profile was created using the lidar equation and the MSISE density data. A signal count of 100 photon counts was assumed at 90 km (Equation 3.1). Then, this simulated profile was used in the normal temperature retrieval program, except this time the effects of overlap were included. Overlap models were calculated similar to those shown in 3.3c, and then the photon counts were multiplied by the inverse of the overlap model. Figure 3.12 is a graph of temperature data affected by overlap models with various tilt angles. As expected, the smaller the laser tilt, the more reliable the data is. The different cases agree at the upper altitudes as expected, as the temperature retrieval starts with the same initial guess. However, the error at the stratopause

increases to about 10 K as the tilt angles increase to 463 μrad. The temperature estimates improve below the stratopause as the overlap in all cases approaches one.

3.5a Real-Time Steering Data

A digital oscilloscope can be used to capture the returned lidar signal. The oscilloscope replaces the multichannel scalar in the receiver allowing the operator to observe the photon count data in real time. A representation of this return is shown in Figure 3.13. This approach works under the assumption that the laser beam divergence and the telescope pointing are precisely known. However, from Figures 3.10 and 3.11, we see that the values of t_1 and t_2 are sensitive functions of telescope tilt and laser beam divergence. A more robust operational approach is to use the lidar echo from a given altitude as a target. The laser beam is steered so as to maximize the amplitude of this echo. In this approach, $\xi(z)$ is maximized in the lidar equation while other parameters remain constant. This approach is insensitive to changes in beam divergence, telescope FOV and telescope pointing. In practice, the overlap observed with the oscilloscope is used to get the laser beam into the telescope FOV and then center the beam in the telescope FOV using the lidar signal from 60-65 km. The altitude is chosen based on two competing factors: (a) a high enough altitude to yield good alignment (a target at infinity would be ideal) and (b) a low enough altitude to yield a statistically significant signal (the lidar signal falls off with altitude and the relative error increases).

On the night of April 7, 2000, the laser and telescope were aligned using this procedure. Once aligned, the laser beam was slowly misaligned and the signal recorded. The variation of total signal from 60-65 km, 50-55 km, and 40-45 km with micrometer setting is shown in Figure 3.14. The uncertainty in the signals is proportional to the square root of the signal. The micrometers allow a

change of 0.01 mm in the tilt of a 70 mm steering mirror, yielding a minimum change in angle of 1/7000 rad or 143 μrad. For this data, the steering has been changed in steps of 0.02 mm or 286 μrad. The laser beam stays in the telescope FOV over 848 μrad (3 steps). With a telescope FOV of 1500 μrad, this suggests a laser beam divergence of 660 μrad, which is in good agreement with the value we have been using of 560 μrad.

The data has been split into two categories: one where the laser is steered toward the telescope and one where the laser is steered away from the telescope. In order to compare this data to an overlap model, it is assumed that the data steered at 8.13 μm has an ideal overlap model, meaning that it is equal to one at all altitudes once it meets up with the telescope FOV. The rest of the data sets were ratioed with this data set and then plotted as seen in Figures 3.15a and 3.16a. A theoretical overlap model was calculated by manually entering the tilt angle of the laser based on the mirror setting. This was done assuming that the angle of the laser at 8.13 microns is zero. The results are shown below in Figures 3.15b and 3.16b and when compared with the real steering data the similarities in the shape and the amount of overlap as the tilt changes are apparent. Note that regardless of the tilt, the bottom 25 km are imperfect due to blanking and pulse pile up. It is also important to note that graphs shown in previous sections, specifically Figures 3.5, 3.10 and 3.11, exhibit the same shape and characteristics as the real steering data for tilting toward the telescope. The negative tilt shown previously in Figure 3.13 exhibits the same shape and characteristics as the real steering data for tilting away from the telescope.

3.5b Overlap and Real Temperature Data

Comparing the actual data to the model overlap temperature function, it can be determined to which nights it would be appropriate to apply the overlap

model. The temperature retrieval program was already programmed to produce the ratio of the actual counts received to the expected counts, termed the overlap ratio. Figure 3.17 provides an example of each of the three main types of overlap ratios encountered. The November 8, 1998 shows a very reliable data set with an overlap model of nearly one at all altitudes. The March 15, 1999 shows a data set that very closely mimics our theoretical overlap models. The January 18, 1999 shows a curved overlap model that is unexplainable in terms of overlap and may be some atmospheric phenomenon or a feature of the arctic atmosphere. If the data's overlap ratio appears to mimic a theoretical overlap model, then that night's data is a good candidate for applying an overlap model filter.

There are four nights chosen for this study: December 30, 1997, January 3, 1998, March 15, 1999 and August 31, 1999. The first three nights are sets of data taken from the Optics Facility and the fourth is taken from the Davis Science Center. The distance between the telescope and the laser has changed between the two locations. Also, in May 1998 the telescope FOV was changed from 1.0 mrad to 1.5 mrad. For the first two nights of data, the steering altitude is 40 km, the telescope FOV is 1.0 mrad, the laser beam divergence is 560 μrad and the distance between the telescope and the laser is 5.93 m. For the third night, the telescope FOV changes to 1.5 mrad. And for the fourth night, the distance between the laser and the telescope changes to 15 m. The first three nights have overlap ratios that are much closer to one than the overlap model. Since these three nights are similar they have been represented by the March 15, 1999 data, shown in Figure 3.18a. The fourth night the overlap model is closer to one than the overlap ratio and is shown in Figure 3.18b. The overlap ratios presented in Figure 3.18 are overlain with various overlap models. It is apparent that the overlap models closely resemble the overlap ratio.

3.6 Discussion and Conclusions

For the purpose of the overlap model, the data is analyzed assuming that the overlap ratio should be equal to one for the atmospheric region of interest. There are some nights of data where the overlap ratio resembles an overlap model and for those nights, there are several possible methods to use for compensation.

Since the overlap model has been calculated and resembles the overlap ratio, one way to look at this problem is to filter the overlap model out of the data. A program takes in the data for the night, calculates the overlap model, multiplies the data by the inverse of the overlap model, and then continues processing the data into temperatures in the usual fashion. This is somewhat unreliable since the exact overlap model cannot be determined precisely; only the best and worst cases can be found. However, when certain data sets are filtered in this fashion the temperature profiles more closely match the MSISE model.

Another way to guarantee an overlap equal to one at all altitudes of interest is as follows. First, align the lidar at the steering altitude using a small pinhole on the receiver. After aligning the lidar, replace the small pinhole with a larger one. Now the laser beam must be in the telescope FOV at every altitude, because its divergence is that much smaller than the telescope FOV. This would be the most sure-fire method of guaranteeing that we are getting the entire reflected signal that is expected. If changing the pinhole size is an impossibility, it is best to steer to as high an altitude as possible. This will ensure that the overlap model is one at least up to that altitude and fairly close to one above.

In the four nights of data shown in the previous section, there are several things to note. The overlap model for the first three nights is much closer to one than the overlap ratio. Filtering the overlap model out in this case, does not result in a temperature profile much closer to the MSISE model. The overlap model for the final data set was a little greater than the overlap ratio. Filtering

this overlap model causes the temperature profile to change drastically and no longer resemble the MSISE model. In general it was found that if the overlap model was worse than the overlap ratio, the temperature profile would change dramatically, and it was best to leave the data unfiltered. When filtering the overlap model out of the data, it worked best when the overlap model was near the overlap function and closer to one than the overlap ratio.

In the lidar system at the Davis Science Center at Poker Flat, the divergence of the laser beam is a relatively unknown parameter. The temperature of the room affects the laser and since there are roof hatches open, this temperature can vary from nearly 80° F to 40° F depending on the time of year and wind conditions. The divergence has been estimated by where the overlap first occurs according to the telescope. An average of all the conjectures was made and the divergence used in this thesis is nearly always equal to 560 μrad. Perhaps if this parameter were better known, a more precise overlap model could be created.

The one parameter found to cause the greatest variance in the overlap models was the distance between the telescope and the laser (x_R). The greater the distance, the more sensitive the overlap model became. Of course the angle of the laser also played an important role, the greater φ_x and the worse the overlap model becomes. There are nights of data where the overlap ratio appears worse than the overlap model. The distance, x_R, cannot be changed, so other parameters might be causing a worse overlap ratio. Perhaps the assumption that the telescope is pointing perfectly vertical is wrong. A short program was written to allow for tilting of the telescope, and it was found that the angle of tilt of the telescope was added to the angle of tilt of the laser and was therefore no different than simply making φ_x larger. There are other more complex issues arising from the laser alignment that could be the cause of the overlap model not correctly following the overlap ratio such as a non-uniform

laser beam or misalignment of the pinhole in the receiving telescope. However, these are beyond the scope of this thesis.

To draw a conclusion based on the basic analysis made here is to say that if the overlap model does not correctly follow the overlap ratio then perhaps there is some unknown event occurring in the atmosphere. However, if the overlap ratio for a specific night of data follows a non-ideal overlap model, that data may be omitted from further processing.

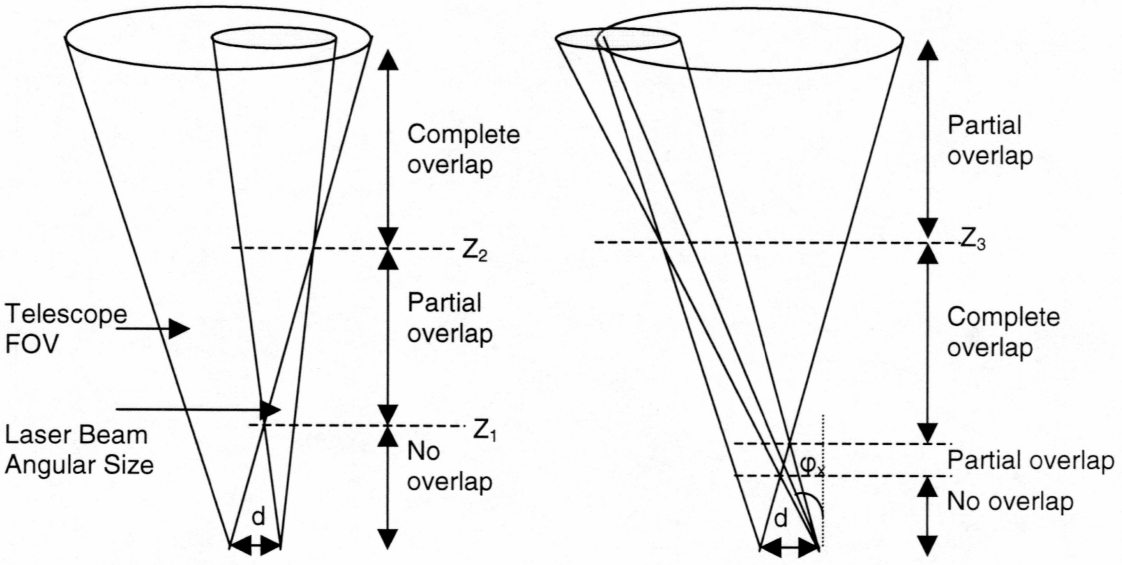

Figure 3.1: Physical overlap of laser beam divergence and telescope FOV for tilted and non-tilted cases.

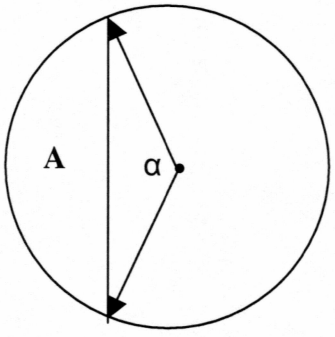

$$A = \tfrac{1}{2}\, r^2(\alpha - \sin\alpha)$$

Figure 3.2: Area of circle portion.

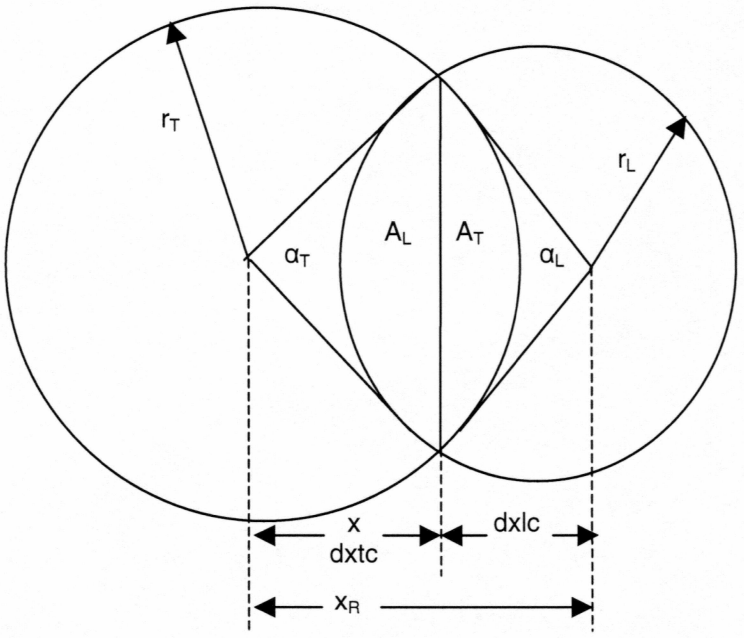

Figure 3.3: Overlap of laser beam divergence and telescope FOV.

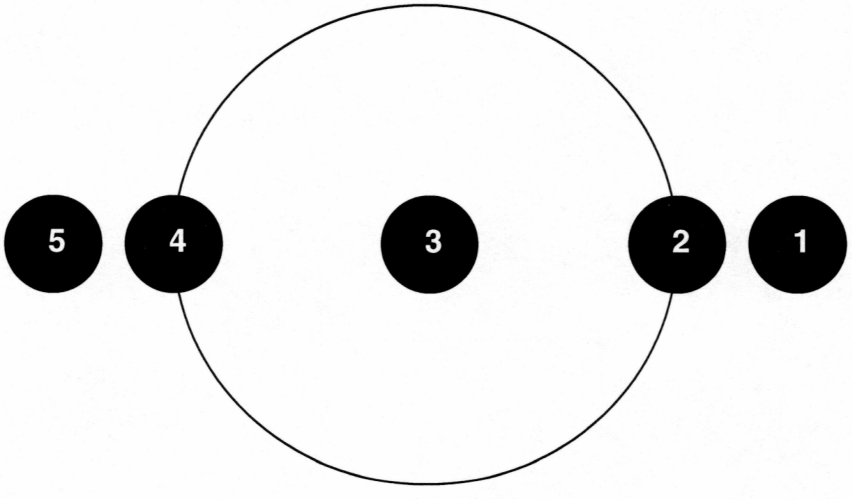

Figure 3.4: Successive views of laser beam moving across telescope FOV in a one direction tilt.

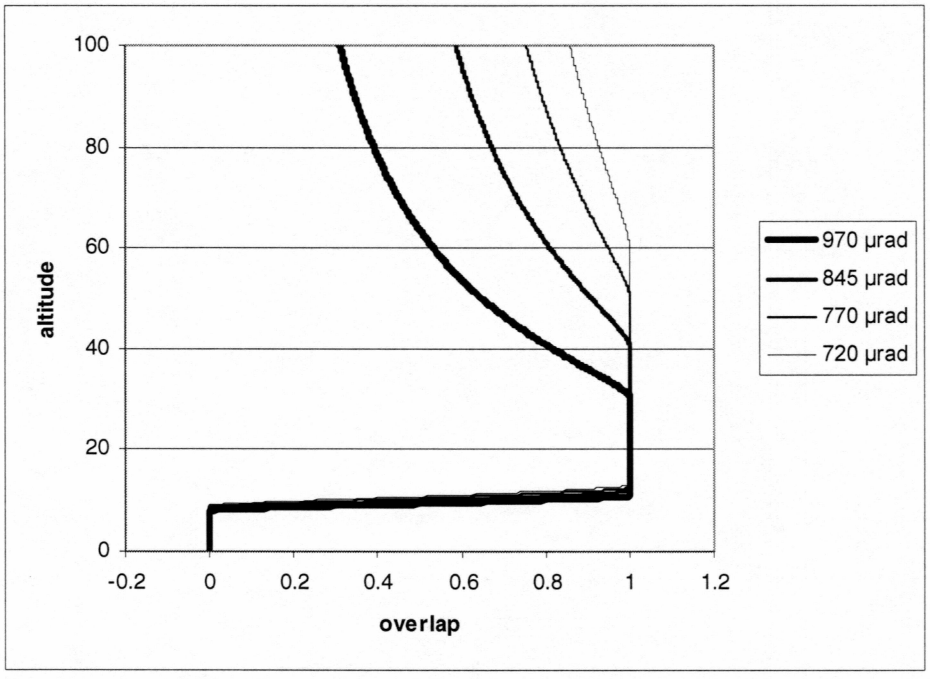

Figure 3.5: Overlap models for various tilt angles in the zenith plane toward the telescope.

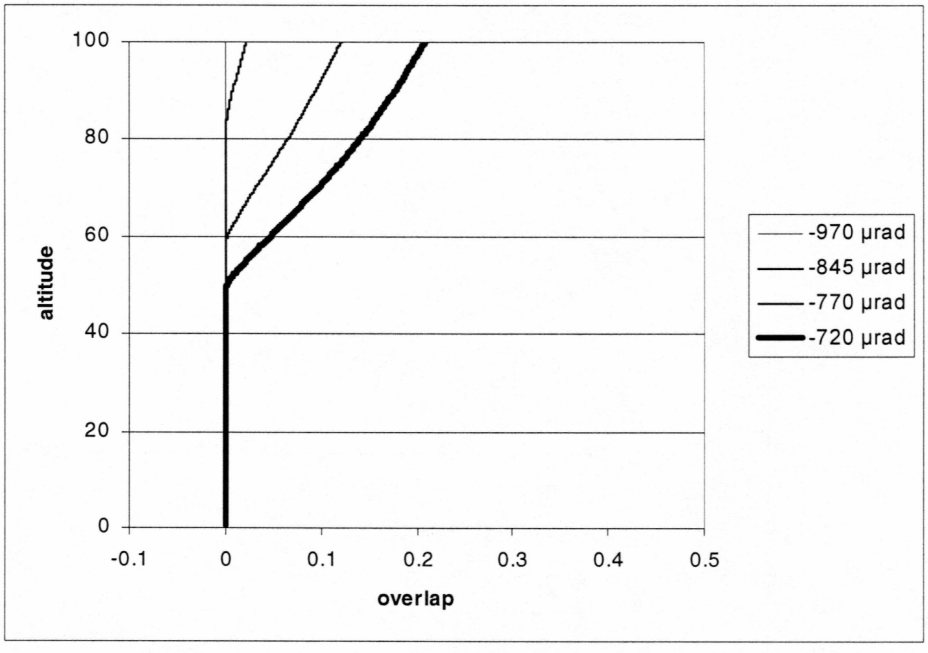

Figure 3.6: Overlap models for various tilt angles in the zenith plane away from the telescope.

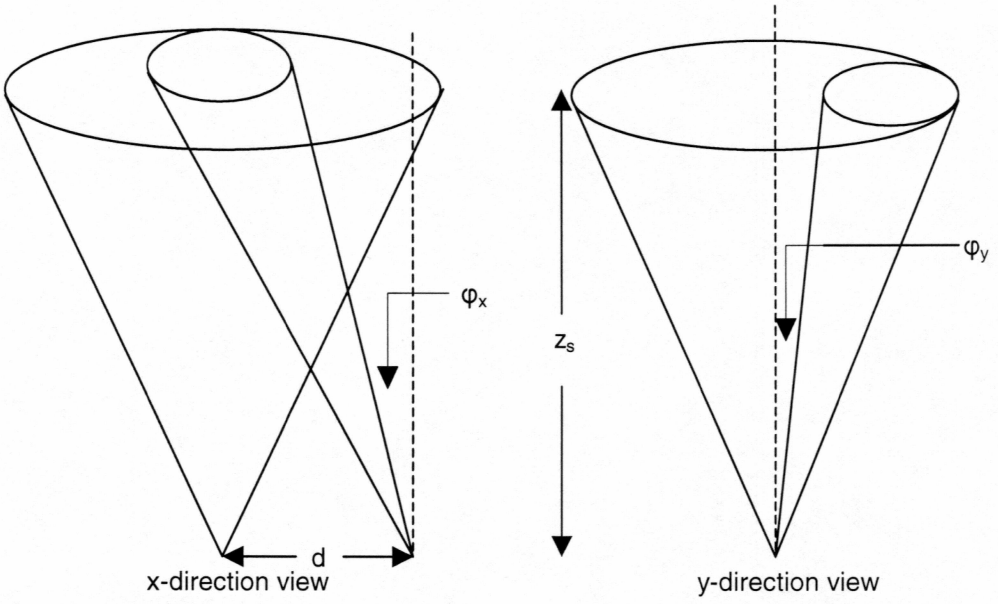

Figure 3.7: x- and y-direction views of overlap out of the zenith plane.

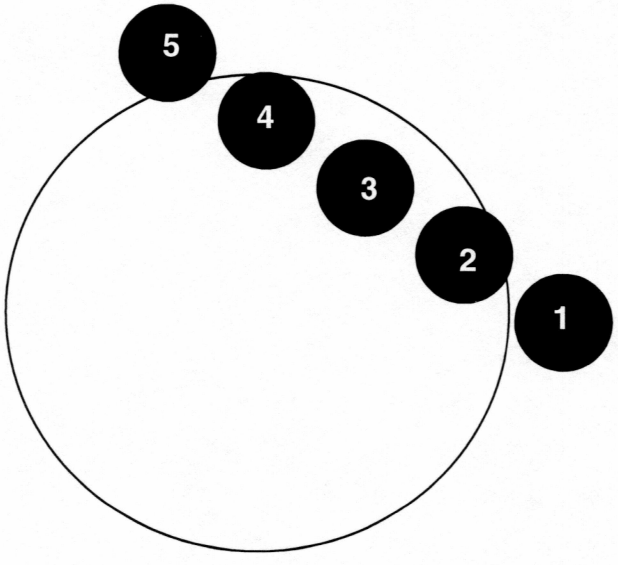

Figure 3.8: Successive views of laser beam moving across telescope FOV in a two direction tilt.

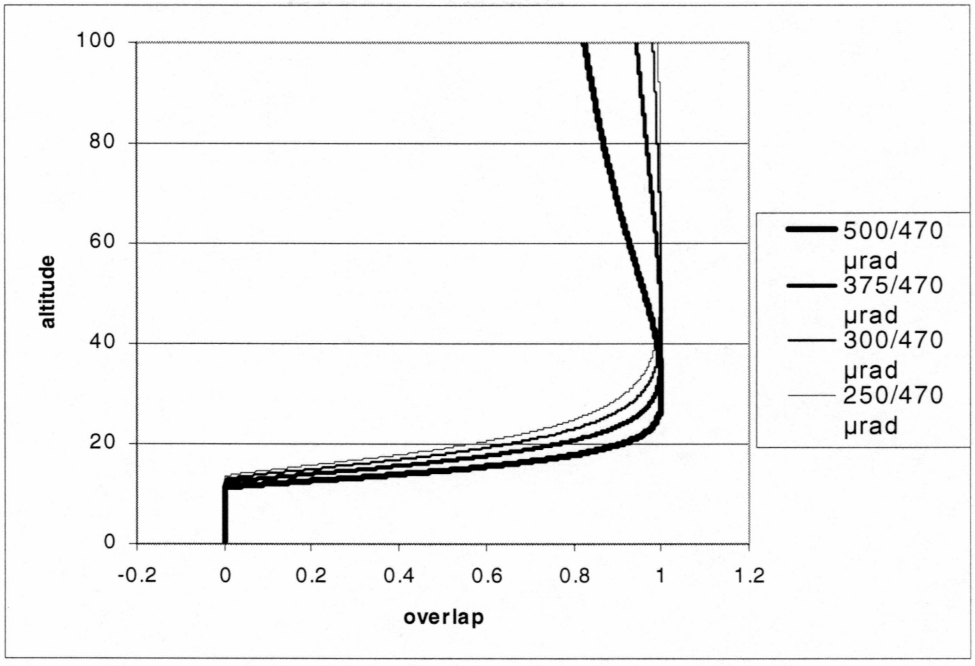

Figure 3.9: Overlap models for various tilt angles out of the zenith plane toward the telescope.

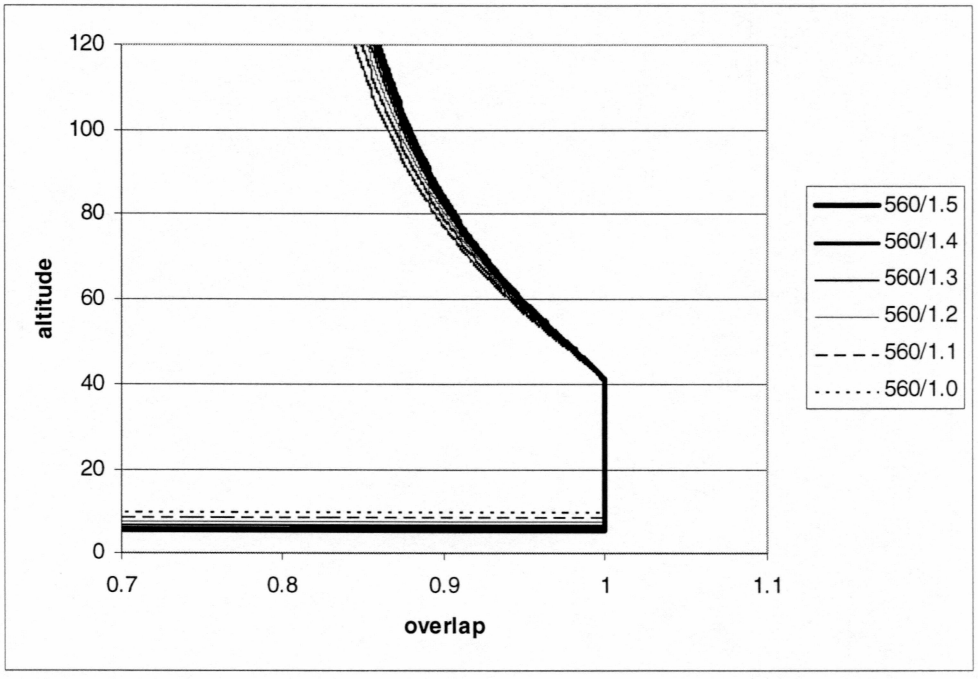

Figure 3.10: Overlap models for various telescope FOVs with constant laser beam divergence.

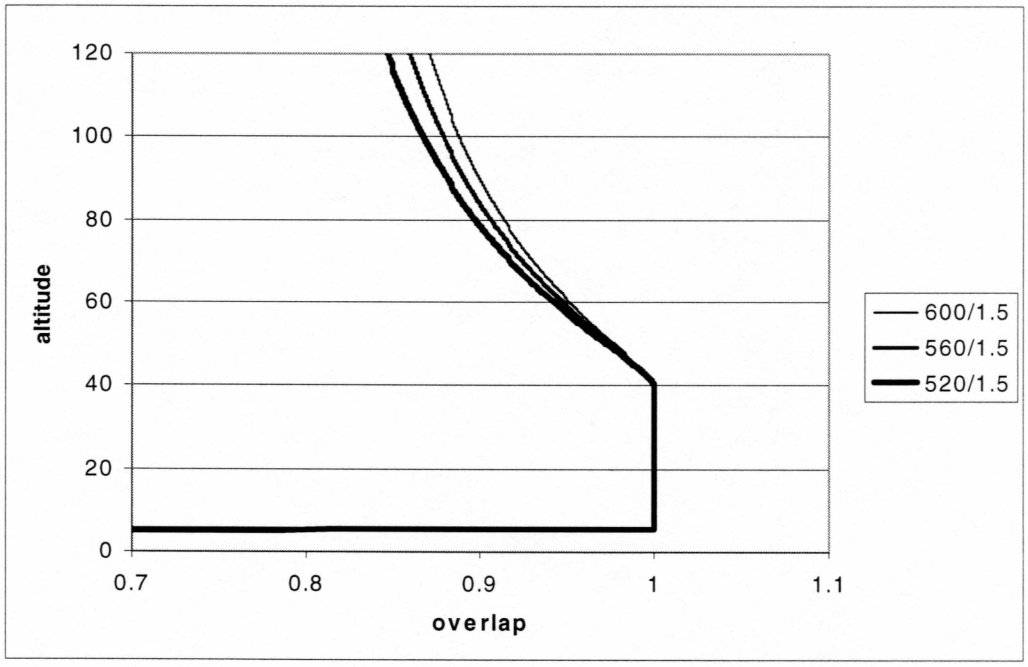

Figure 3.11: Overlap models for various laser beam divergences with constant telescope FOV.

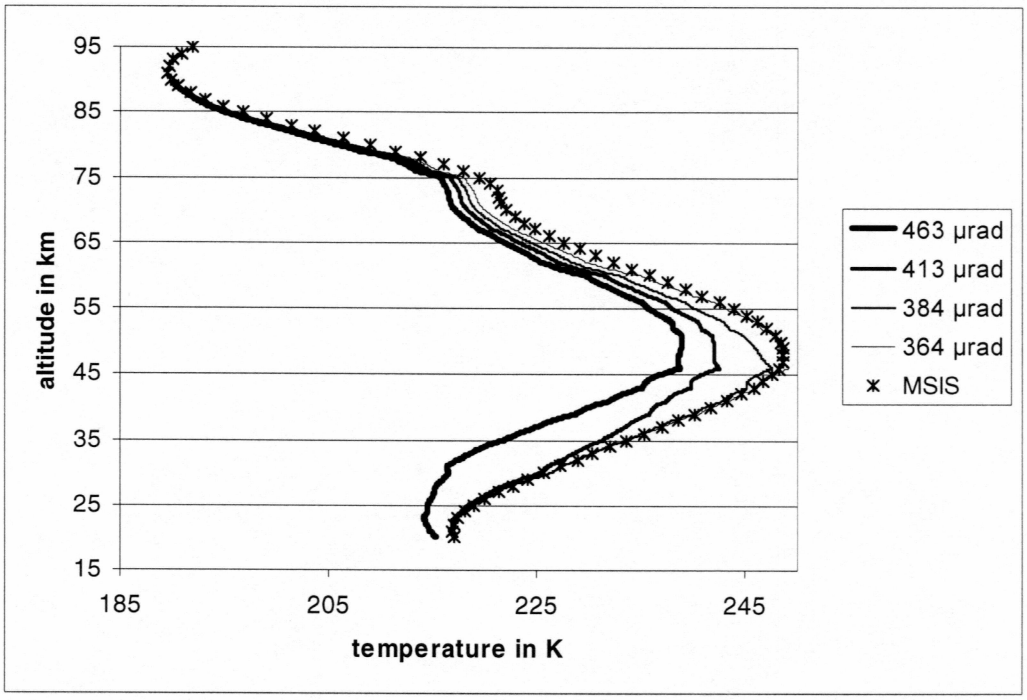

Figure 3.12: Effects of non-ideal overlap function on temperature retrieval.

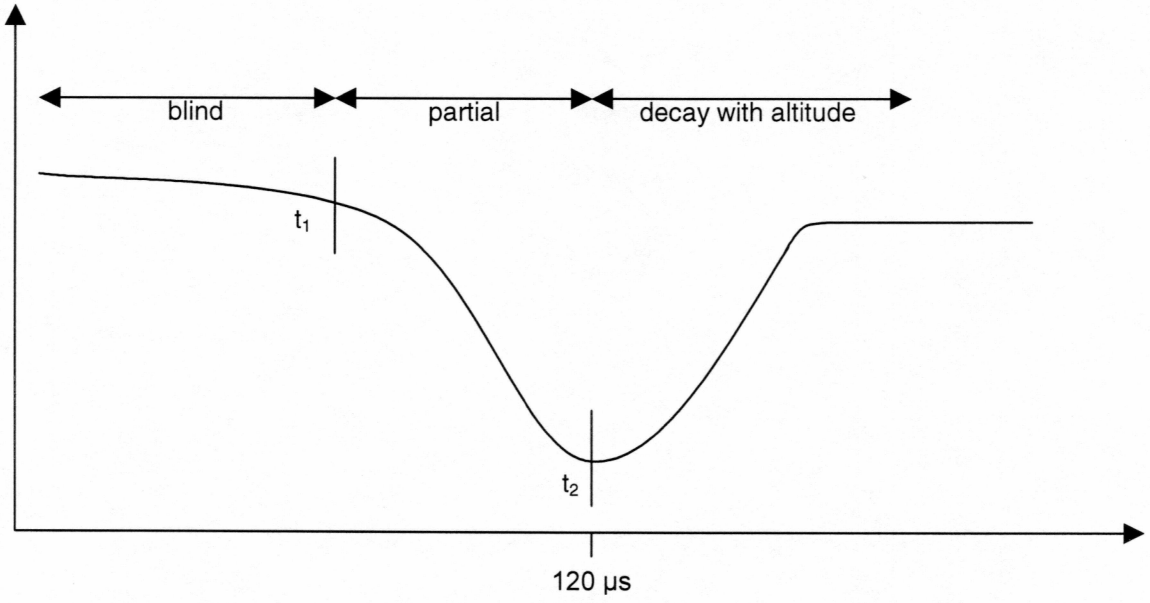

Figure 3.13: Lidar return on oscilloscope.

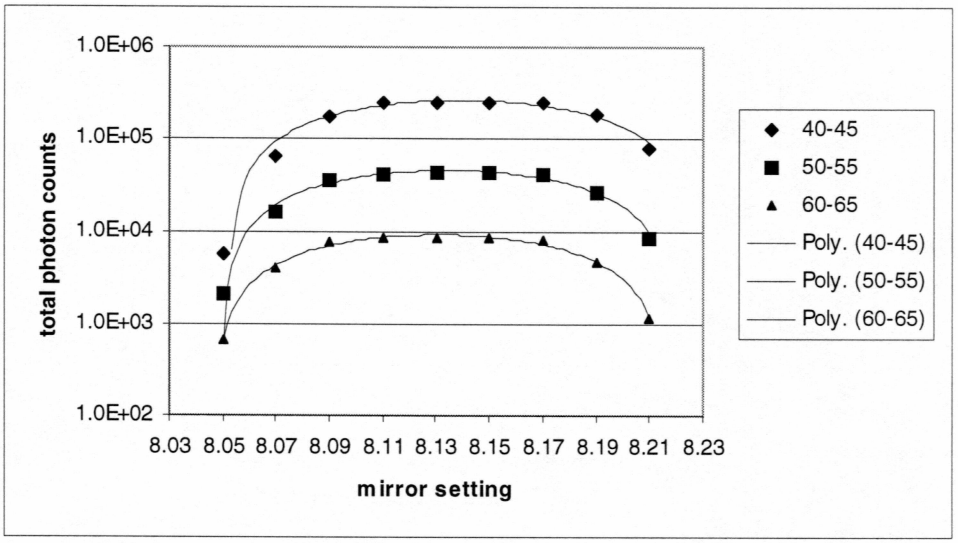

Figure 3.14: Number of photon counts at various altitudes according to mirror setting.

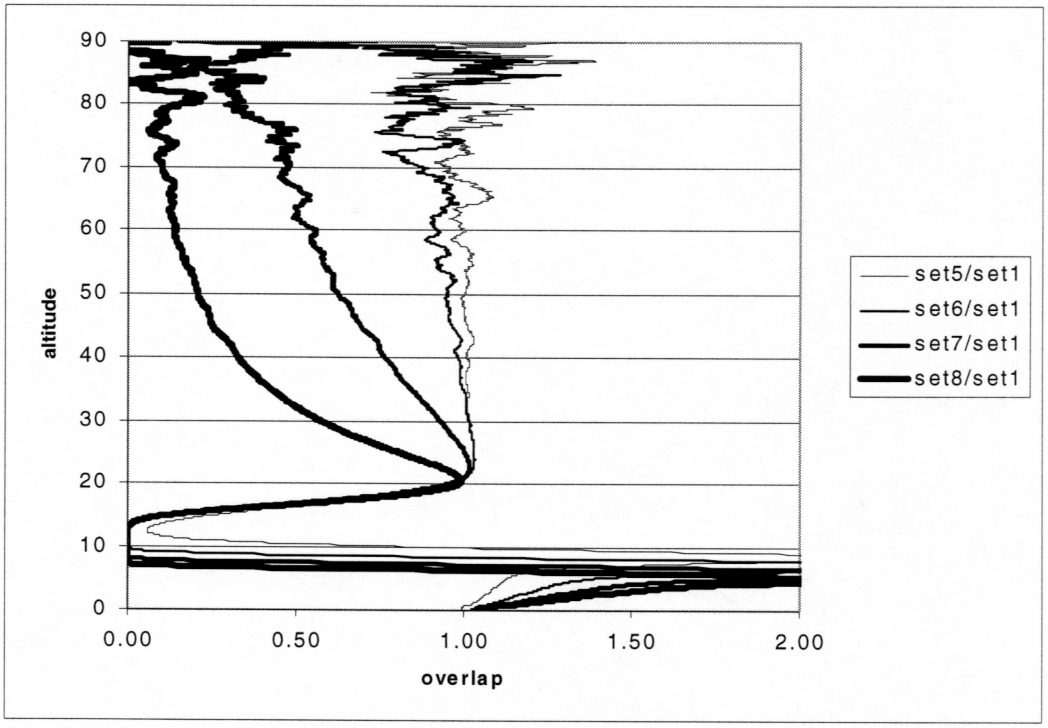

Figure 3.15a: Ratio of sets tilted toward telescope.

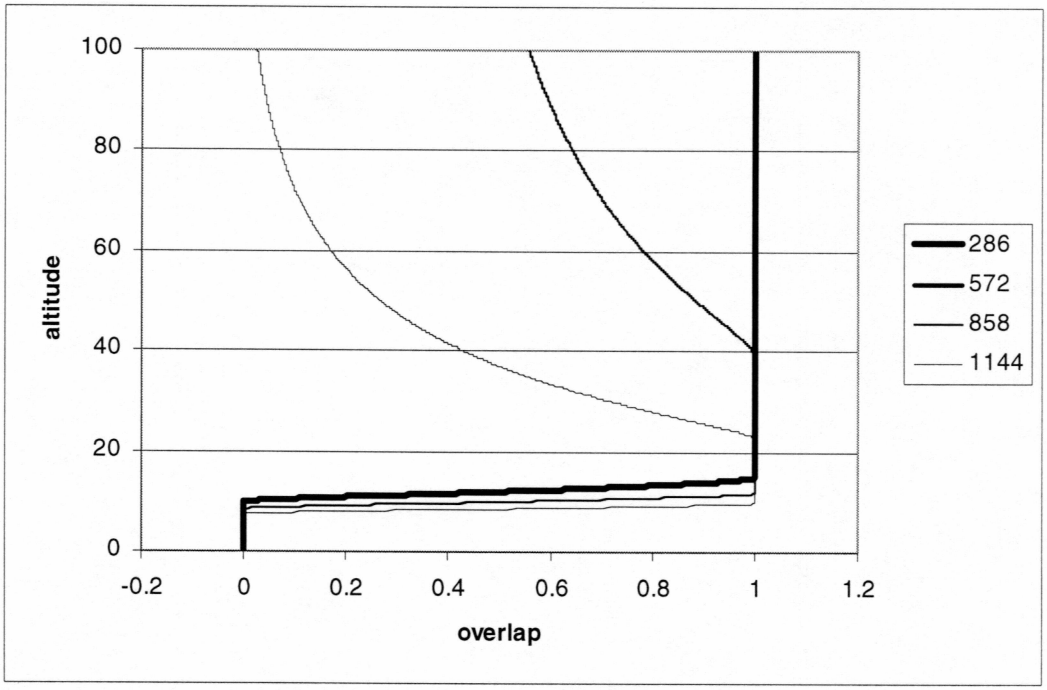

Figure 3.15b: Overlap models for tilting (in μrad) toward telescope.

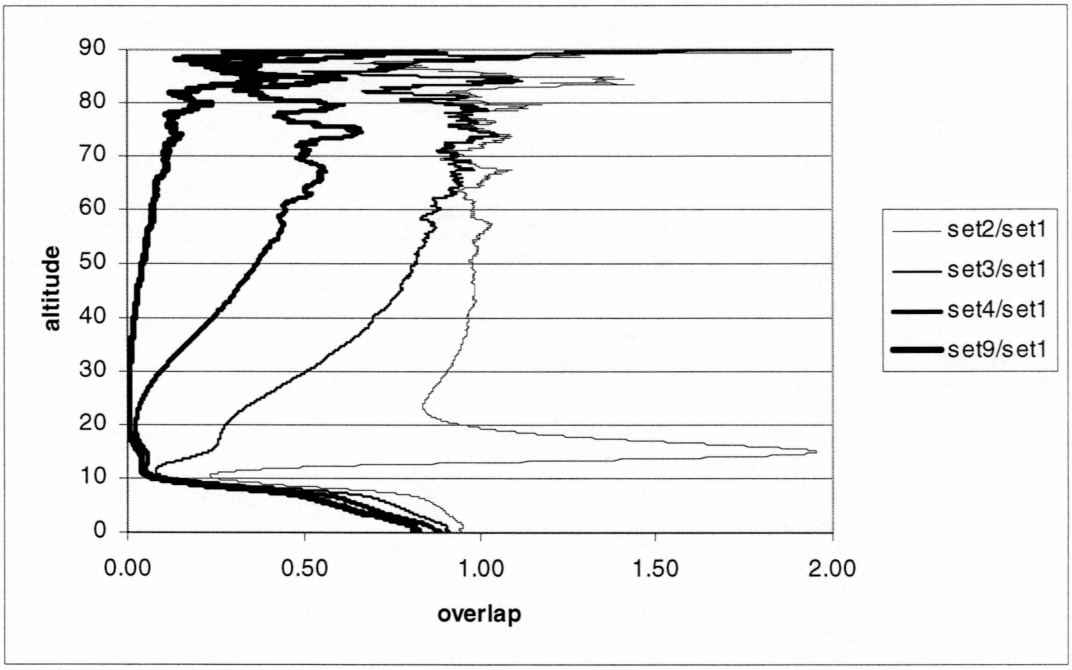

Figure 3.16a: Ratio of sets tilted away from telescope.

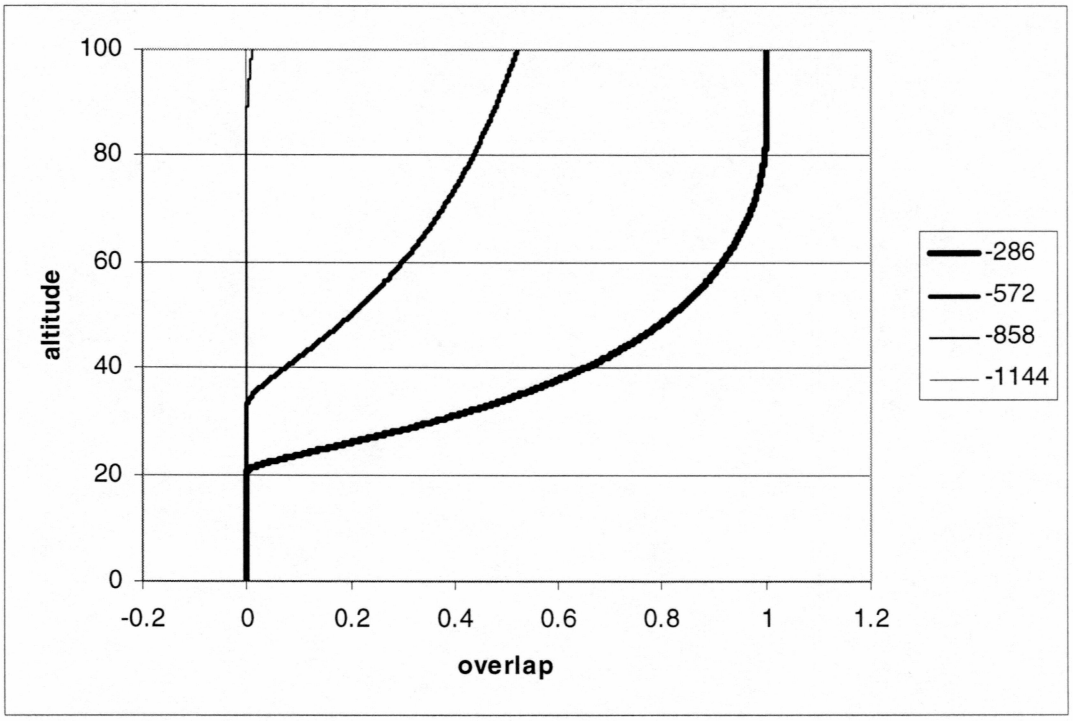

Figure 3.16b: Overlap models for tilting (in μrad) away from telescope.

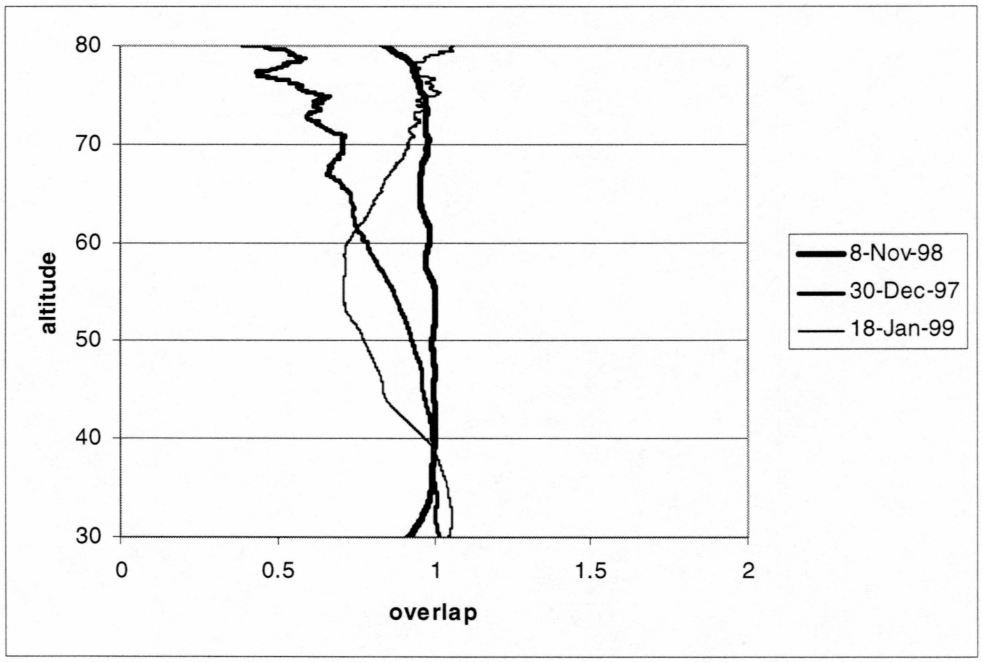

Figure 3.17: Examples of various types of overlap ratios.

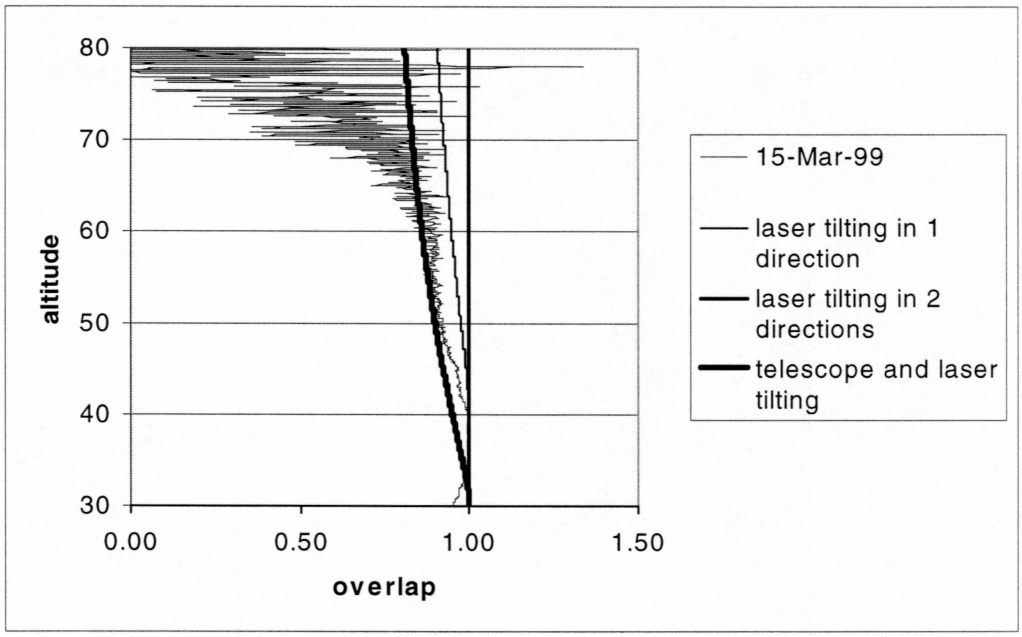

Figure 3.18a: March 15, 1999 overlap ratio overlain with various overlap models.

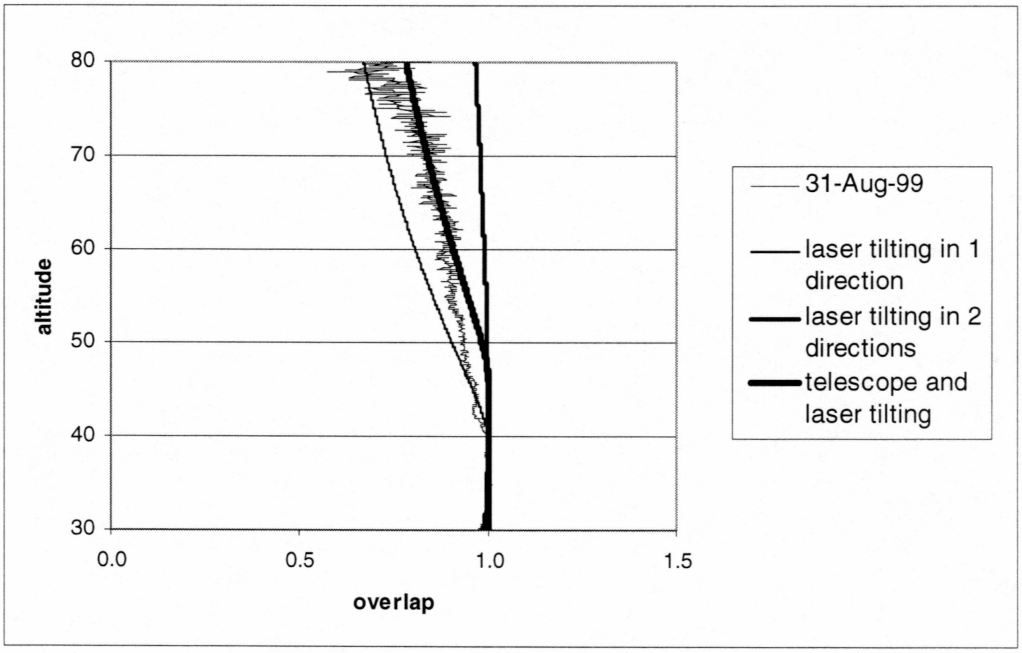

Figure 3.18b: August 31, 1999 overlap ratio overlain with various overlap models.

Chapter 4: Temperature Observations at Poker Flat Research Range

4.1 Introduction

The CRL Rayleigh lidar was operated during nighttime on 41 occasions between November 14, 1997 and April 8, 2000 at Poker Flat Research Range (PFRR). Of these 41 observations, 34 were of sufficient duration (> 2 hours) and data quality to yield temperature profiles. Thus the temperature data presented in this thesis represents 270 hours of observations obtained between August and April over a 2.5-year period. PFRR is located at 65°N, therefore the solar elevation is too high between April and August to yield useful measurements. Figure 4.1 shows the distribution of observations through the year.

The general thermal structure of the atmosphere (see Figure 1.1) is illustrated by the PFRR observations. A measured temperature profile observation for October 11, 1999 is shown in Figure 4.2 where the temperature profile is plotted against altitude. The profile shows increasing temperature up to 50 km and then decreasing temperature above 50 km. The maximum at 50 km is the stratopause. Smaller scale local maxima and minima are also evident in the observation. The stratopause is maintained by solar heating of ozone, as it absorbs nearly all the ultraviolet radiation between 240 and 290 nm. Ozone absorption also provides a significant energy source for driving the circulation of the mesosphere, and for forcing tides in the upper mesosphere and thermosphere [Wayne, 1985]. In an ozone-free atmosphere (e.g., the Martian atmosphere) the planet surface is the warmest feature and the temperature falls off with altitude from the surface. On Earth, the temperature initially falls off with altitude in the troposphere (~0-15 km). Above the tropopause, the temperature is first nearly constant, then increases in the stratosphere (~15-55 km) due to ozone heating. Radiative processes dominate the stratosphere, leading to its

layered structure. The temperature reaches a maximum near 50 km, known as the stratopause. Above the stratopause the temperature once again decreases with altitude in the region known as the mesosphere (~55-100 km). Above 100 km the atmosphere again warms with altitude due to absorption by hard-UV radiation by oxygen. Thus the tropopause and mesopause appear as local temperature minima while the stratopause appears as a maximum. Given this simple radiative explanation for the thermal structure of the atmosphere and the fact that sunlight is apparently necessary for ozone heating, the persistence of the stratopause in polar winter is an unexpected feature. Kanzawa [1989] and Holton [1983] show that the persistence of the polar winter stratopause can only be explained by a small-scale wave breaking effect in the middle atmosphere. For each night of data, the stratopause temperature and altitude were determined from the average profile. Then, these results were averaged by month. MSISE models in 1 km intervals were generated for the middle of each month and the stratopause temperatures and altitudes were determined and then compared to the PFRR data. These results are shown in Figure 4.3 and it is apparent that the PFRR data (individual points) follows the MSISE model.

4.2 Inversion layers

Occasionally, an inversion layer occurs above the stratopause when the atmospheric lapse rate becomes positive for a brief period as seen in Figure 4.2. According to MSISE or other model atmospheres, the lapse rate above the stratopause should be negative. These layers are termed mesospheric inversion layers (MIL) as they have a temperature inversion on their bottomside. MILs typically occur between 55 and 70 km with an average temperature depth of 8.5 K. Figure 4.2 shows an inversion layer with a maximum near 68 km. LeBlanc and coworkers [1997] have extensively studied MILs at the Observatoire de Haute Provence (OHP), France (44°N, 6°E) over the mid-latitudes. They report

inversion layers at an altitude of 70 km in the winter and 80 km in the summer. LeBlanc and coworkers find a positive gradient at the bottom of the inversion layer is found to be typically 3-5 K/km regardless of the type of inversion layer event. Whiteway and coworkers [1995] also have observed MILs at Toronto, Canada (44°N, 80°W). They find the MILs at mid-latitudes with overlying nearly adiabatic lapse rates, which indicate a well-mixed atmosphere. The MILs observed by Whiteway and coworkers, were found near 55 km in midwinter and 80 km in summer and they noted that their mesospheric thermal structure was different from that of Hauchecorne and coworkers [1987]. Both studies conclude that the MIL is a common feature at midlatitudes. They are observed nearly 70% of the time during winter and 30% of the time during the summer at these midlatitude sites.

Table 4.1: MIL characteristics.

Date	Topside lapse rate (K/km)	Inversion layer gradient (K/km)	Stratosphere lapse rate (K/km)	Peak altitude (km)	Depth (km)	Amplitude (K)	Duration (hr)	Maximum amplitude (K)
November 14,1997	-3.1	2.2	-1.8	59.2	2.0	3.9	6.8	9.4
March 3, 1998	-4.2	1.5	-2.9	54.6	1.7	2.1	10.4	5.5
November 8, 1998	-3.1	1.1	-2.1	58.5	1.8	1.6	10.2	12.0
October 11, 1999	-3.9	6.3	-2.2	67.6	3.1	16.5	5.4	33.3
November 15, 1999	-2.0	4.4	-2.9	59.1	3.3	11.7	6.0	29.5

From the observations at PFRR MILs have been detected on 5 occasions. Three of these five occasions are in November when seven observation sets exist. Curiously, none exist during December and January when twelve observations exist. Note that eight of these observations periods fall in January 1999. While Figure 4.2 shows a strong inversion layer over a 5-hour period, Figure 4.4 shows the evolution of a MIL in a sequence of 2-hour temperature profiles on November 8, 1998. The characteristics of these layers are summarized in Table 4.1. Following LeBlanc and coworkers [1997] the depth of the inversion, the amplitude of the inversion and the topside and bottomside lapse rates were determined. The lapse rate found above the stratopause and below the inversion layer was determined by fitting a line to the points between 1 km above the stratopause and 1 km below the inversion minimum. The lapse rate found above the inversion layer was determined by fitting a line to the points between 1 km above the inversion layer maximum and a set of altitudes 3-12 km above the inversion layer maximum. The 1 km cutoffs serve to reduce the error due to edge effects of the lapse rate changing sign. Several lapse rates were thus determined and the one with the smallest root mean square error was the one chosen to represent the lapse rate above the inversion layer. The positive gradient found between the inversion layer minimum and maximum was determined by using all points between the minimum and maximum. The 1 km cutoffs could not be implemented for the positive gradients because the depth of the inversion layers was less than 2 km in some cases. In 1991, the Improved Stratospheric And Mesospheric Sounder (ISAMS) instrument aboard the Upper Atmosphere Research Satellite (UARS) satellite shows inversion layers over Alaska during December [LeBlanc et al., 1995]. This study is the first time lidar has been used to identify inversion layers at high latitudes. On several nights of data taken at PFRR, MILs appear, confirming the ISAMS observation. These observations are in good agreement with other observations made by satellite

and by other lidars (e.g., LeBlanc and Whiteway). Figure 4.5 shows the temperature profile for the night of October 11, 1999 with lapse rates overlying the data.

4.3 Discussion of Observations

The general structure of the stratopause follows that of the MSISE model at 65°N. MILs are observed though less frequently than reported at midlatitudes. The topside lapse reported in this lidar study are not close to adiabatic as reported by Whiteway and coworkers, who find an overlying adiabatic lapse rate of –9.8 K/km. The PFRR observations show MIL topside lapse rates that are similar to those on the topside of the stratopause (~3.8 K/km). However the peak altitudes are similar to those reported by Whiteway and coworkers [Whiteway et al., 1995]. The average positive gradient found between the inversion layer minimum and maximum is an average of 3.5 K/km, which is in good agreement with LeBlanc and coworkers [1997]. This study confirms the ISAMS satellite study of LeBlanc and coworkers [1995]. The satellite observations show MILs covering areas of Alaska in December 1991.

The physical mechanism underlying MILs is not completely understood. [Meriwether and Gardner, 2000 and references therein] However, recent models suggest that the phenomenon is due to interactions between tides and waves. [Liu et al., 2000] These studies have focused on the interaction between the diurnal tide and gravity waves. The PFRR observations are consistent with that view. The frequency of MILs at PFRR is significantly less at this high latitude (65°N) site than at midlatitude sites. This is consistent with the fact that the diurnal (24 hour) tide is significantly damped at these high latitudes where the local inertial period is 13.2 hours. In fact the appearance of MILs at these high latitude sites may reflect a semi-diurnal (12 hour) or ter-diurnal (8 hour) tidal influence on the formation of these layers.

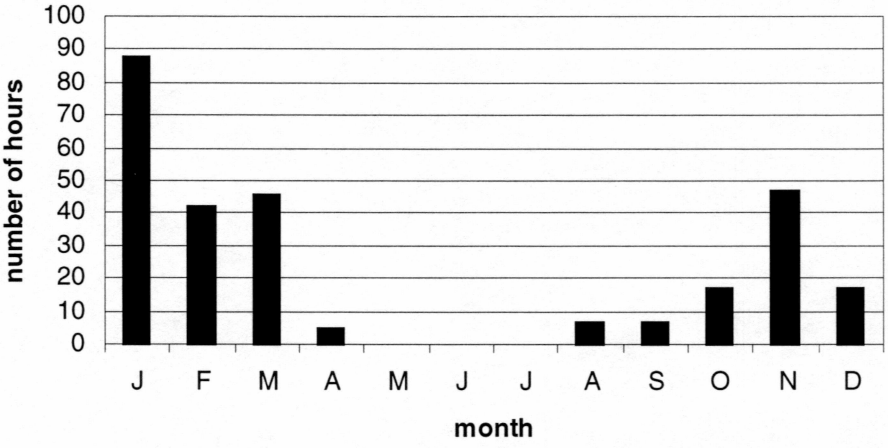

Figure 4.1: Distribution of lidar observations by month.

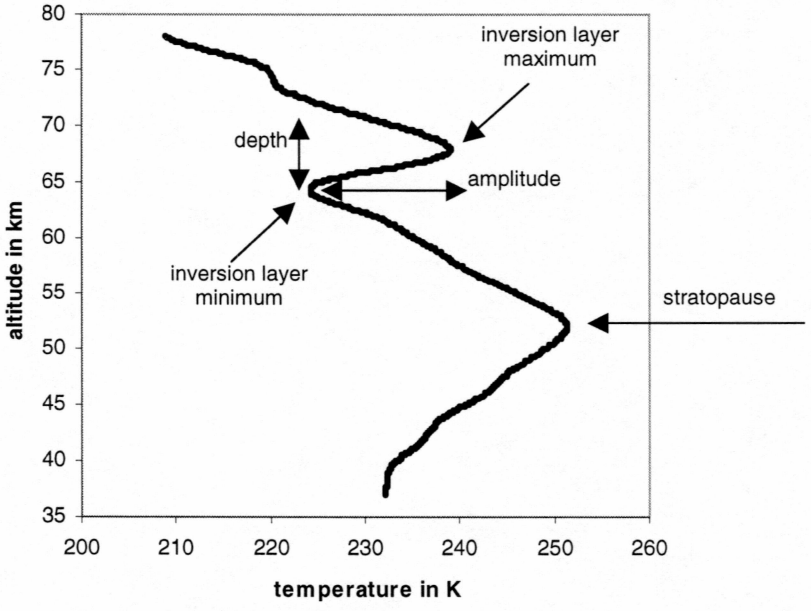

Figure 4.2: Typical data from October 11, 1999 showing middle atmosphere features.

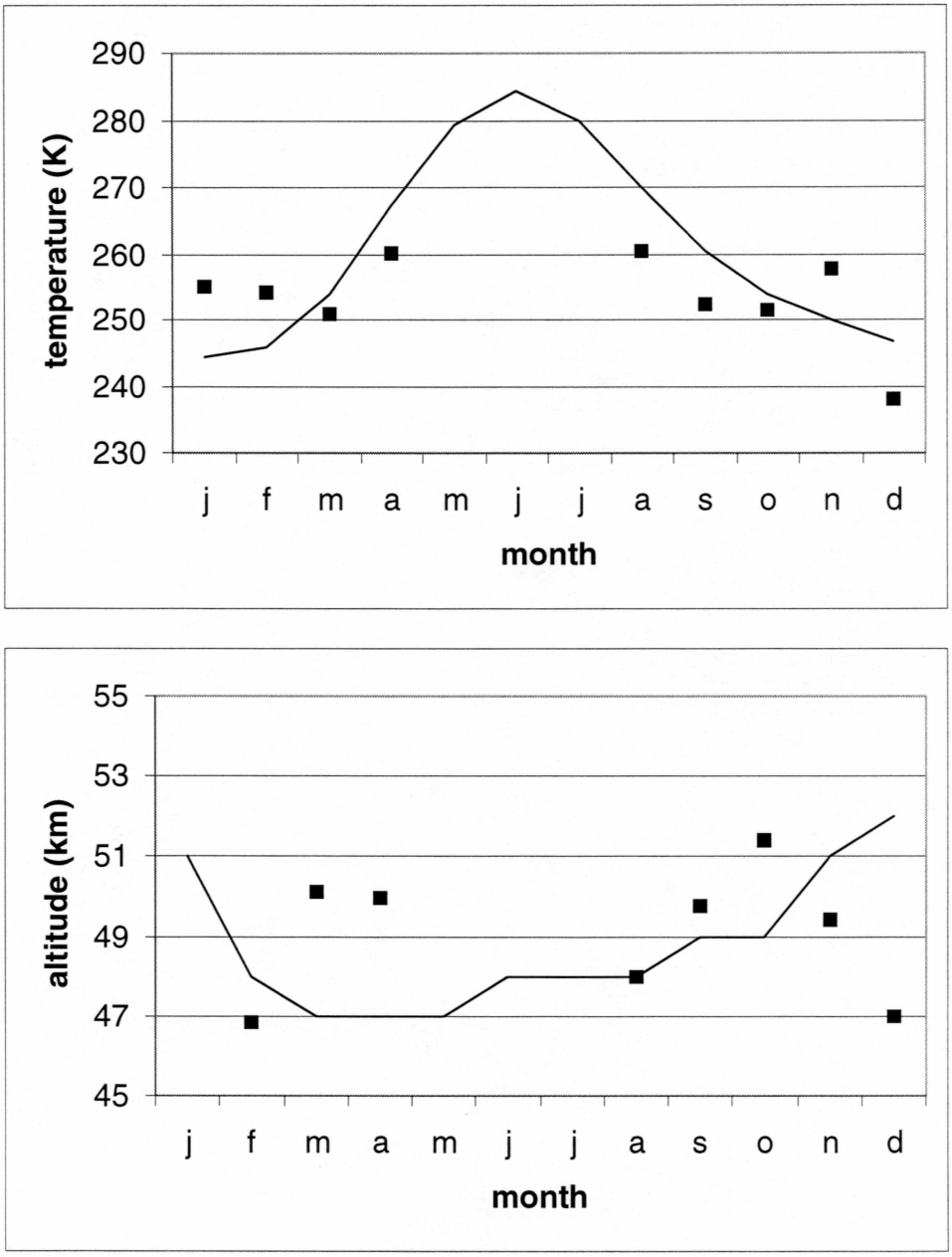

Figure 4.3: Comparisons of PFRR data with MSISE model for stratopause temperature and altitude.

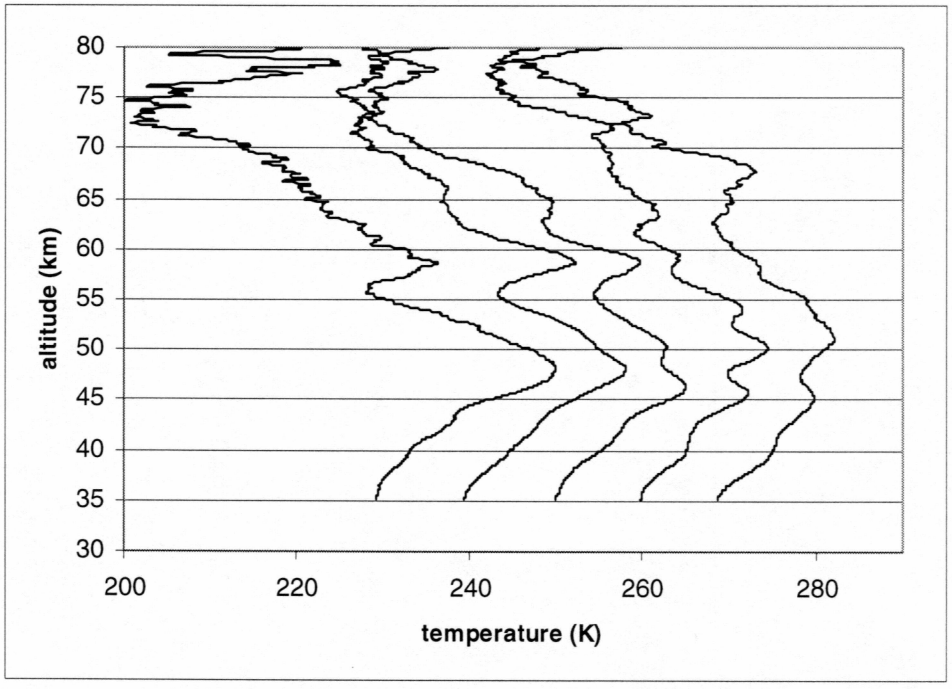

Figure 4.4: 2-hour sequential (from left) temperature profiles from November 8, 1998.

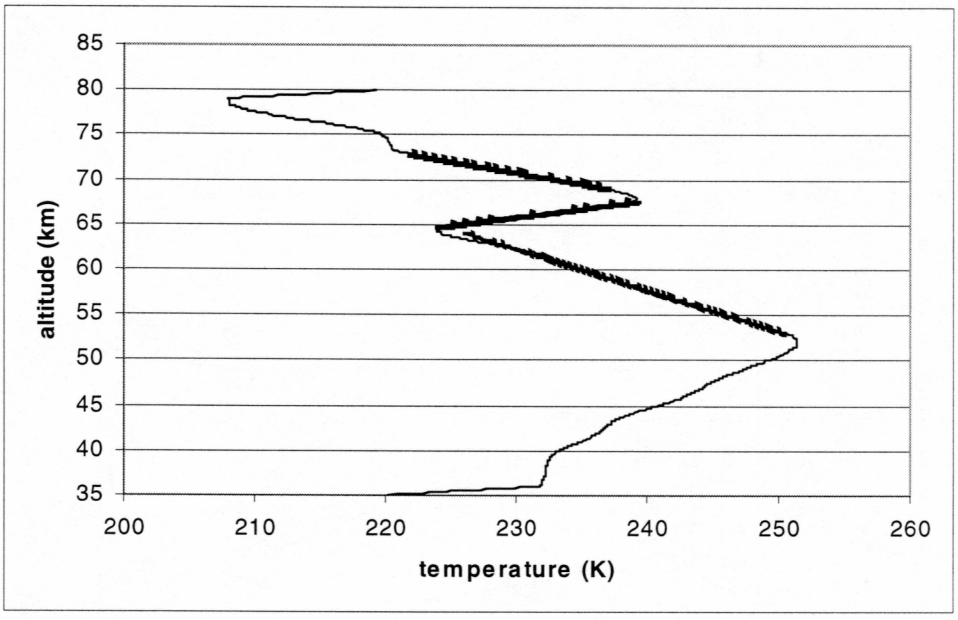

Figure 4.5: Lapse rate fitting to the temperature profile of the night of October 11, 1999.

Chapter 5: Conclusions and Recommendations for Further Work

This thesis presents the initial engineering analysis of a new laser radar system at PFRR and a presentation of the first science results. The CRL Rayleigh lidar system at PFRR is photon count limited in its noise behavior as shown by the spectral analysis. The effects of the receiver and transmitter alignment are considered. A technique for how data might be screened is proposed. However, the move to new lidar facility will improve these alignment issues by providing better stability in the floors and lab temperature. To continue the work on alignment, the precise laser beam divergence and how it varies as a function of temperature should be found.

The lidar system is capable of observing small-scale inversion features in the upper mesosphere. These features are less common than at midlatitudes. This difference may reflect difference in tidal components between these sites. More work is needed in comparing the PFRR data set to other data sets as well as investigating the causes behind the inversion layers such as tides and the polar vortex. The 1995 ISAMS satellites study was independently confirmed, which indicated inversion layers over Alaska. Data sets should be obtained more frequently in the winter at the new lidar facility. These observations will provide a more accurate picture of the appearance and disappearance of MILs and allow studies of the polar vortex in the Western Arctic.

Appendix A: Hydrostatic Equilibrium

The lidar equations assume hydrostatic equilibrium throughout the atmosphere. The assumption is that, in the vertical direction, the most important forces acting on a parcel of air are the vertical pressure gradient and gravity. A short program was written to test this assumption. The test is performed on the MSISE 1990 and CIRA 1986 files. If these are reasonably small, then the PFRR data is reliable because these models are used as a comparison. It also provides a chance to look at the models.

The hydrostatic approximation is:

$$\frac{dp}{dz} = -\rho(z)g(z). \tag{B.1}$$

The model files provide density, pressure and altitude. The acceleration due to gravity can be calculated at each altitude using:

$$\frac{g_0}{(1.0+\frac{z}{R_E})^2}, \tag{B.2}$$

where $g_0 = 9.8 m/s^2$. The hydrostatic ratio, ε, can be calculated from:

$$\varepsilon = \frac{\Delta P}{\rho g \Delta z}, \tag{B.3}$$

where the ideal ratio, ε, is equal to one. Figure B.1 shows the CIRA 1986 model at 5km resolution. The ratio varies between 0.95 and 1.05 except for a spike at 80km. This spike, as explained in Appendix B, is due to two models being joined at that altitude with possible discontinuities. Figure B.2 shows the MSIS 1990 model at 5km resolution. The ratio varies between 0.99 and 1.04 with no spikes.

Note that the ratio due to the hydrostatic equilibrium assumption is much greater than the error found in Appendix B.

MSISE 1990 is more consistent with hydrostatic equilibrium than CIRA 1986. It is also based on one model, not two, like CIRA 1986. Therefore this model has been used as a comparison for the PFRR data.

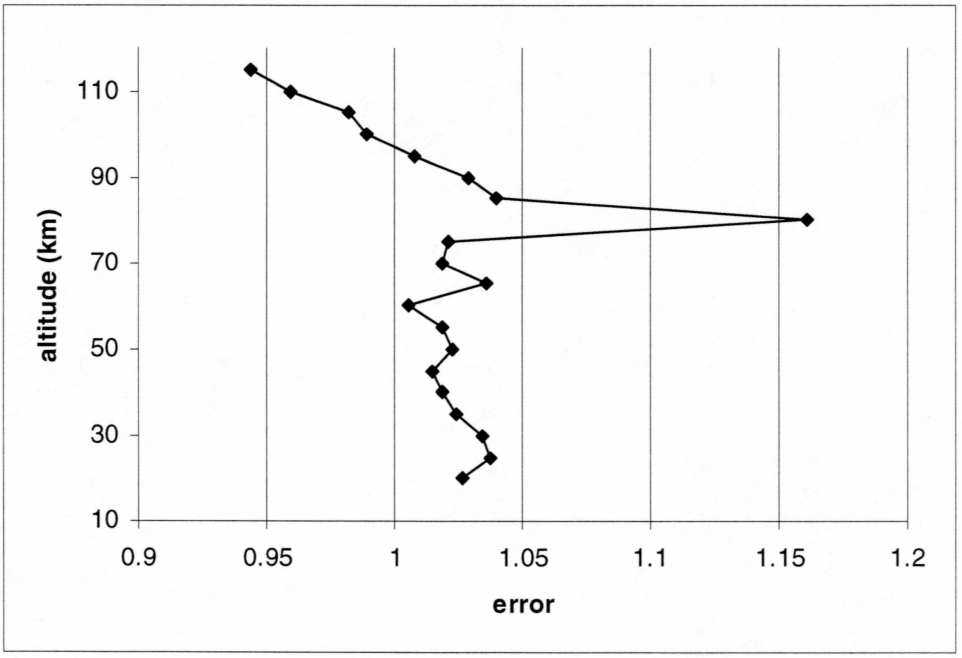

Figure A.1: CIRA 1986 errors

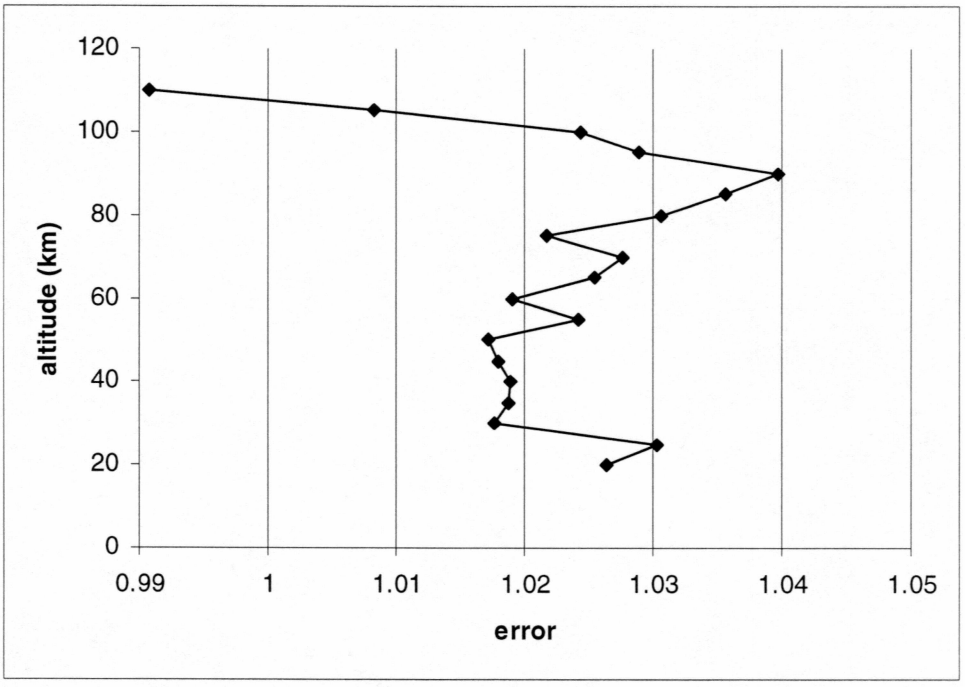

Figure A.2: MSISE 1990 errors

Appendix B: Testing Rayleigh Lidar Technique with Model Atmospheres

A possible source of error looked at was the temperature models. These models are used for two main purposes. One is to seed the temperature profiles in the main temperature processing program. The other purpose is to compare it with the calculated temperature profile. The model files used were created from both the COSPAR International Reference Atmosphere (CIRA) 1986 and the Mass Spectrometer Incoherent Scatter (MSISE) 1990 models. The MSISE 1990 model was created from the CIRA 1986, MSIS 1986 and newer results for a model that reaches across several atmospheric boundaries. The CIRA model is based on observations. The MSISE model is based on previous models, observations and an ideal atmosphere, which assumes a hydrostatic isothermal atmosphere.

A program was created to investigate different aspects of the model files. The model files used were both at 1 km and 5 km resolution. The models provide density, pressure and temperature. Using only the density, simulated photon count data sets were created from these models by using the lidar equation. The photon count data sets were extended from the model files into either 0.1 km or 0.5 km resolution. These finer resolutions correspond to linear interpolation between the model's density points. These simulated photon count data sets were then used to create a temperature profile, which is then compared to the model temperature. The model data points were overlaid onto the temperature profile. Ideally the model points should have exactly overlapped with the false data set that had been created since they were based on the same model, except that one was reprocessed through the lidar equation. However,

small discrepancies were found between the original model points and the reprocessed model.

Previously the CIRA 1986 model had been used for comparison with the PFRR data. These files have pressure and temperature at 5 km height intervals. They worked reasonably well, but through close scrutiny, it was noted that there is often a spike or discrepancy at the 80 km mark. It was found that two different models that are combined to form the CIRA 1986 model meet up at 80 km and this was the cause of the discrepancy. As long as the calculations were seeded at 80 km or lower, this discrepancy did not come into play. If the calculations were seeded above 80 km, the spike would appear. This spike is noticeable in Table A.1 whenever the CIRA models are seeded at 90 km. First, the CIRA model was extended to 0.1 km resolution instead of the 0.5 km previously used to see if the smaller intervals would get rid of the discrepancy at 80 km. The smaller resolution had less error, but that error was almost imperceptibly different between the two resolutions. Next, a geometric mean height technique was looked at. A new model using the CIRA model was created. This time a geometric mean was used on two adjacent 5 km intervals in hopes that this would provide a better average over the range bin. This technique resulted in the greatest errors.

Finally, the MSISE model at 1 km intervals and at 5 km intervals was used. The MSISE model is created using a method that continues through 80 km so there isn't the large discrepancy that CIRA had. The greater the model resolution was and the greater the calculation resolution was, the greater the errors were. It seems that using the initial 5 km resolution and the 0.1 km calculation resolution is best. Overall, using the MSISE model gave smaller errors than the CIRA model and did not show a large spike at the 80 km altitude. Table A.1 summarizes these findings. For comparison with the PFRR data, the MSISE 1990 model was used at 5 km resolution, as it was the most consistent.

Table B.1: MSISE and CIRA model study results.

model	model resolution (km)	resolution of calculations (km)	start altitude (km)	20 km error	stratopause error	rms error
MSISE-90	1	0.1	90	0.3	8E-02	8E-02
MSISE-90	1	0.1	80	0.3	8E-02	7E-02
MSISE-90	1	0.1	70	0.3	8E-02	6E-02
MSISE-90	1	0.5	90	0.2	4E-02	7E-02
MSISE-90	1	0.5	80	0.2	5E-02	7E-02
MSISE-90	1	0.5	70	0.2	5E-02	5E-02
MSISE-90	5	0.1	90	0.2	-5E-05	3E-01
MSISE-90	5	0.1	80	0.2	1E-02	2E-01
MSISE-90	5	0.1	70	0.2	3E-02	2E-01
MSISE-90	5	0.5	90	0.2	-3E-02	3E-01
MSISE-90	5	0.5	80	0.2	-2E-02	2E-01
MSISE-90	5	0.5	70	0.2	2E-03	2E-01
CIRA-86	5	0.1	90	-0.2	-6E-01	2E+01
CIRA-86	5	0.1	80	-0.2	-3E-01	3E-01
CIRA-86	5	0.1	70	-0.2	-4E-01	3E-01
CIRA-86	5	0.5	90	-0.2	-6E-01	2E+01
CIRA-86	5	0.5	80	-0.2	-4E-01	3E-01
CIRA-86	5	0.5	70	-0.2	-4E-01	3E-01

Appendix C: Temperature Error Analysis

In the main temperature processing program, the error in the temperature is also calculated. This error provides the uncertainty in the final calculated temperature. The lidar measures the photon counts, *N*, and the altitude, *z*, is known. Since the temperature, *T*, is calculated from these two quantities and some constants (Equation C.1), the uncertainty in *T* is based on the uncertainty in both *N* and *z*.

$$T_i = \frac{T_1 N_1 z_1^{\,2}}{z_i^{\,2} N_i} + \frac{M}{R}\Delta z \sum_{j=2}^{i} \frac{N_j g_j z_j^{\,2}}{z_i^{\,2} N_i} \tag{C.1}$$

For the initial temperature term, T_1, the uncertainty is based on the uncertainty in the photon counts, N_0, at the initial altitude, z_0. The relative error in the initial term is calculated in Equations C.2 through C.6.

$$\frac{\Delta T_1^{\,2}}{T_1^{\,2}} = \frac{\Delta x^2 + \Delta y^2}{(x+y)^2} \tag{C.2}$$

where,

$$x = \frac{T_0 N_0 z_0^{\,2}}{N_1 z_1^{\,2}}, \tag{C.3}$$

$$\frac{\Delta x^2}{x^2} = \left[\frac{\Delta T_0^{\,2}}{T_0^{\,2}} + \frac{\Delta N_0^{\,2}}{N_0^{\,2}} + \frac{\Delta N_1^{\,2}}{N_1^{\,2}} + \right], \tag{C.4}$$

$$y = \frac{M}{R}\Delta z g_1, \tag{C.5}$$

and

$$\frac{\Delta y^2}{y^2} = 0. \tag{C.6}$$

When being processed into temperature, the data is smoothed by a certain range. The usual smoothing range used on the PFRR data is 2 km. Therefore, there are independent points only at every 2 km, the points in between are now dependent on those 2 km points. Next, the relative errors in the whole temperature array are calculated using a similar procedure to that of calculating the initial error. Only the independent points are used in the uncertainty calculations to prevent the propagation of errors from the dependent points. The dependent points were previously included and created large uncertainties.

$$\frac{\Delta T_j^{\,2}}{T_j^{\,2}} = \frac{\Delta N_j^{\,2}}{N_j^{\,2}} + \frac{\Delta C^2 + \Delta B^2}{(B+C)^2} \tag{C.7}$$

where,

$$B = \frac{T_0 N_0 z_0^{\,2}}{z_j^{\,2}}, \tag{C.8}$$

$$\frac{\Delta B^2}{B^2} = \frac{\Delta T_0^{\,2}}{T_0^{\,2}} + \frac{\Delta N_0^{\,2}}{N_0^{\,2}}, \tag{C.9}$$

$$C = \frac{M\Delta z}{R} \sum_{i=1}^{j} \frac{N_i z_j^{\,2}}{z_i^{\,2}} g_i, \tag{C.10}$$

and

$$\Delta C^2 = \left(\frac{M\Delta z}{R}\right)^2 \sum_{i=1}^{j} \Delta N_i^{\,2} \left(\frac{z_j}{z_i}\right)^4 g_i^{\,2}. \tag{C.11}$$

The square of the uncertainty is calculated at these independent points and then linearly interpolated. An example of the temperature profile and associated error from the night of November 8, 1998 is plotted in Figure C.1. The thick black line is the temperature and the dashed lines indicate the uncertainty in the temperature. Clearly, the small inversion layer (discussed in Chapter 4) near 58 km is significant.

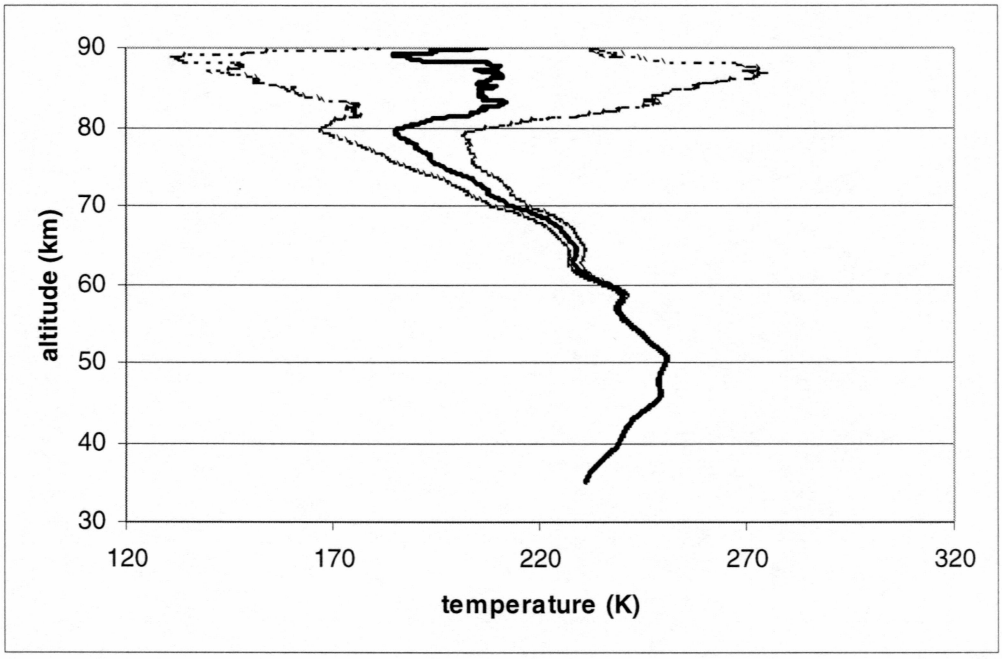

Figure C.1: Temperature profile with uncertainty.

References

1. Bevington, P.R., "Data Reduction and Error Analysis for the Physical Sciences", McGraw-Hill, Inc., 1969.
2. Bilitza, D., MSISE 1990 Atmosphere Model [Online], available: http://nssdc.gsfc.nasa.gov/space/model/models/msis.html, accessed: August 16, 2000.
3. Bills, R.E., C.S. Gardner, C.-Y. She, Narrowband lidar technique for sodium temperature and Doppler wind observations of the upper atmosphere, Optical Engineering, 30, 13-21, 1991.
4. Blackman, R.B., J.W. Tukey, "The Measurement of Power Spectra", Dover Publications, NY, NY, 1958.
5. Chanin, M.L., Review of lidar contributions to the description and understanding of the middle atmosphere, Journal of Atmospheric and Terrestrial Physics, 46, 987-993, 1984.
6. Chen, S., Z. Hu, M.A. White, H. Chen, D.A. Krueger, C.Y.She, Lidar observations of seasonal variation of diurnal mean temperature in the mesopause region of Fort Collins, Colorado (41°N, 105°W), Journal of Geophysical Research, 105, 12,371-12,379, 2000.
7. Collins, R.L., D. DeLucia, M. Piedra, S.M. Thomas, T. Itabe, K. Mizutani, Collaborative Lidar Studies of the Arctic Middle Atmosphere, 49th Arctic Science Conference, 25-28 October, Fairbanks, AK, 1998a.
8. Collins, R.L., D. Lummerzheim, R. W. Smith, Analysis of lidar systems for profiling aurorally excited molecular species, Applied Optics, 36, 6024-6034, 1997.
9. Collins, R.L., D.C. Senft, C.S. Gardner, Observations of a 12 h wave in the mesopause region at the South Pole, Geophysical Research Letters, 19, 57,60, 1992
10. Collins, R.L., J. Breese, T. Itabe, K. Mizutani, Joint GI and CRL Lidar Observations at Poker Flat Research Range, International Workshop on the Arctic Atmosphere Observation, December 15-17, Tokyo, Japan, 1998b.
11. Duck, T.J., J.A. Whiteway, A.I. Carswell, A detailed record of High Arctic strato-mesospheric temperatures, Journal of Geophysical Research, in press to appear 2000.
12. Dutton, J. A., "The Ceaseless Wind", Dover Publications, Inc. NY, NY, 1976.

13. Elterman, L., The measurement of stratospheric density distribution with the searchlight technique, Journal of Geophysical Research, 56, 509-520, 1951.
14. Goody, R., "Principles of Atmospheric Physics and Chemistry", Oxford University Press, Inc., NY, NY, 1995.
15. Goody, R.M., Y.L. Yung, "Atmospheric Radiation Theoretical Basis", Oxford Univeristy Press, NY, NY, 1989.
16. Hauchecorne, A., and A. Maillard, a 2-D dynamical model of mesospheric temperature inversions in winter, Geophysical Research Letters, 17,2197-2200, 1990.
17. Hauchecorne, A., and A. Maillard, The Mechanism of Formation of inversion layers in the mesosphere, Advance Space Research, 12, (10)219-(10)223, 1992.
18. Hauchecorne, A., M.L. Chanin, Density and temperature profiles obtained by lidar between 35 and 70km, Geophysical Research Letters, 7, 565-568, 1980.
19. Hauchecorne, A., M.L. Chanin, P. Keckhut, Climatology and trends of the middle atmospheric temperature (33-87 km) as seen by Rayleigh lidar over the south of France, Journal of Geophysical Research, 96, 15,297-15,309, 1991.
20. Hauchecorne, A., M.L. Chanin, R. Wilson, Mesospheric Temperature Inversion and Gravity Wave Breaking, Geophysical Research Letters, 14, 933-936, 1987.
21. Hecht, J., "The Laser Guidebook", McGraw-Hill, Inc., 1992
22. Holton, J.R., The influence of gravity wave breaking on the general circulation of the middle atmosphere, Journal Atmospheric Science, 40, 2497-2507, 1983
23. Kanzawa, H., Warm Stratopause in the Antarctic Winter, Journal of the Atmospheric Sciences, 46, 435-438, 1989.
24. Keckhut, P., A. Hauchecorne, M.L. Chanin, Midlatitude long-term variability of the middle atmosphere: trends and cyclic and episodic changes, Journal of Geophysical Research, 100, 18,887-18,897, 1995.
25. Kent, G.S., R.W. Wright, A review of laser radar measurements of atmospheric properties, Journal of Atmospheric and Terrestrial Physics, 32, 917-943, 1970.
26. Kong, J. A., "Electromagnetic Wave Theory", John Wiley & Sons, Inc., 1986.
27. Leblanc, T., A. Hauchecorne, M.L. Chanin, R.W. Taylor, C.D. Rodgers, and N. Livesey, Mesospheric temperature inversions as seen by ISAMS in December 1991, Geophysical Research Letters, 22, 1485-1488, 1995.

28. Leblanc, T., A. Hauchecorne, Recent observations of mesospheric temperature inversions, Journal of Geophysical Research, 102, 19,471-19,482, 1997.
29. Leblanc, T., I.S. McDermid, A. Hauchecorne, P. Keckhut, Evaluation of optimization of lidar temperature analysis algorithms using simulated data, Journal of Geophysical Research, 103, 6177-6187, 1998.
30. Liu, H.-L., M.E. Hagan, R.G. Roble, Local mean state changes due to gravity wave breaking modulated by the diurnal tide, Journal of Geophysical Research, 105, 12,381-12,396, 2000.
31. Measures, R. M., "Laser Remote Sensing: Fundamentals and Applications", Krieger Publishing Company, Malabar, FL, 1984.
32. Meriwether, J.W., C.S. Gardner, A review of the mesospheric inversion layer phenomenon, Journal of Geophysical Research, 105, 12,405-12,416, 2000.
33. Meriwether, J.W., P.D. Dao, R.T. McNutt, W. Klemetti, W. Moskowitz, G. Davidson, Rayleigh lidar observations of mesospheric temperature structure, Journal of Geophysical Research, 99, 16,973-16,987, 1994.
34. Meriwether, J.W., X. Gao, V.B. Wickwar, T. Wilkerson, K. Beissner, S. Collins, M.E. Hagan, Observed coupling of the mesospheric inversion layer to the thermal tidal structure, Geophysical Research Letters, 25, 1479-1482, 1998.
35. Oppenheim, A.V., R.W. Schafer, "Discrete-Time Signal Processing", Prentice Hall, Inc., 1989.
36. Papoulis, A., Probability, Random Variables, and Stochastic Processes, McGraw-Hill, New York, 1984.
37. Rayleigh, On the light from the sky, its polarization and colour, Phil. Mag., LXI, 107-120, 274-279, 1871.

References

38. Rise, Set and Twilight Definitions [Online], available: http://aa.usno.navy.mil/AA/faq/docs/RST_defs.html, accessed: August 16, 2000.
39. Salby, M.L., "Fundamentals of Atmospheric Physics", Academic Press, Inc., 1996.
40. She, C.Y., J.R. Yu, D.A. Krueger, R. Roble, P. Keckhut, A. Hauchecorne, M.L. Chanin, Vertical structure of the midlatitude temperature from stratosphere to mesopause (10-105 km), Geophysical Research Letters, 22, 377-380, 1995.
41. Solomon, P.A., K.L. Magliano, The 1995 Integrated Monitoring Study (IMS95) of the California Regional PM10/PM2.5 Air Quality Study (CRPAQS): study overview, Atmospheric Environment, Oxford, England, 33, 4747-4968, 1999.

42. Stokes, G.G., On the dynamical theory of diffraction, Cambridge Phil. Transactions, 7, 1-62, 1849.
43. Sun or Moon Altitude/Azimuth Table for One Day, USNO Astronomical Applications Department [Online], available: http://aa.usno.navy.mil/AA/, accessed: August 16, 2000.
44. Synge, E.H., A method of investigating the higher atmosphere, Phil. Mag., 9, 1014-1020, 1930.
45. Van de Hulst, H.C., "Light Scattering by Small Particles", Dover Publications, Inc., NY, NY, 1981.
46. Wayne, R.P., "Chemistry of Atmoshperes", Oxford University Press, 1985.
47. Whiteway, J.A., A.I. Carlswell, and W.E. Ward, Mesospheric temperature inversions with overlying nearly adiabatic lapse rate: An indication of a well-mixed turbulent layer, Geophysical Research Letters, 22, 1201-1204, 1995.